Satellite Microwave Radar Observations of Antarctic Sea Ice

Mark R. Drinkwater

Jet Propulsion Laboratory, MS 300-323
California Institute of Technology
4800 Oak Grove Drive
Pasadena, CA 91109
USA

Submitted to: *"Recent Advances in the Analysis of SAR for Remote Sensing of the Polar Oceans"* Chapter 8.
by C. Tsatsoulis and R. Kwok (Eds.)

Publisher: Springer-Verlag, New York.

Final Draft Submitted: November 21, 1996

Satellite Microwave Radar Observations of Antarctic Sea Ice

Mark R. Drinkwater

Jet Propulsion Laboratory
California Institute of Technology
4800 Oak Grove Drive
Pasadena, CA 91109

Abstract

Since 1991, the European Space Agency's two ERS satellites have acquired microwave radar data of Antarctica. ERS data have been recorded by two receiving stations, one German, one Japanese. The former has allowed direct downlink and recording of high bit-rate, high resolution SAR image data of the Weddell and Bellingshausen Seas during station campaigns. The latter has enabled some data from the Cosmonaut Sea and Indian Ocean quadrant to be collected.

The Active Microwave Instrument (AMI) on board ERS has two modes; SAR and Scatterometer. When the AMI is not an imaging mode, it allows backscatter data to be acquired when direct SAR downlink is not possible, or when the receiving station is inoperable. Recent advances in image generation from Scatterometer data enable complementary medium-scale resolution images to be made from the ERS-1 Scatterometer mode data during times when SAR images cannot be acquired. Together, these combined C-band microwave image data for the first time enable uninterrupted coverage of this geographic region at both high (25m) and medium-scale (-12 km) resolutions.

A selected C-band dataset collected within the time period 1992-1994 are analyzed, with the main focus placed on 1992 data coinciding with Ice Station Weddell (ISW) and Winter Weddell Gyre Study (WWGS '92) field experiment data acquisition. The main characteristics of Antarctic ice signatures are pointed out, together with some of the contrasts between Southern Ocean and Arctic ice. Results show large differences with the typical range of C-band backscatter coefficients recorded in the Arctic. Similarly, seasonal changes show dramatic differences, with ice floes undergoing different geophysical processes. Sea-ice dynamic processes are investigated under two contrasting regimes; coastal and central Weddell Sea ice. Drift characteristics in response to geostrophic wind forcing differ depending upon the internal ice stresses which are applied. A large proportion of the Southern Ocean ice pack responds in near "free-drift", however, and examples are provided of the spatial and temporal response of the ice to long-term synoptic and episode forcing. The drift of ISW and surrounding ice floes, and several buoys during WWGS'92 are examined and the performance of the ice tracker evaluated.

These active microwave radar observations in the Southern Ocean are contributing towards revolutionizing the study of Antarctic sea-ice geophysics. Seasonal patterns of sea-ice drift together with the transitions in sea-ice characteristics are being characterized, and the longer the high-resolution temporal records are available, the better the chances of investigations of climate-related interannual variability.

Table of Contents

1. INTRODUCTION 1

2. OBTAiNING SPACEBORNE RADAR DATA IN ANTARCTICA 2

2.1 ANTARCTIC SAR DATA 2

2.1.1 *ERS-1 and ERS-2 SAR* 2

2.1.2 *J-ERS-1 SAR* 2

2.1.3 *Radarsat SAR* 2

2.1.4 ERS SAR *Backscatter Calibration Accuracy* 3

2.2 ANTARCTIC SAR RECEIVING STATIONS 3

2.3 SCATTEROMETER IMAGING 4

3. SAMPLING ISSUES 4

3.1 TEMPORAL AND SPATIAL COVERAGE 4

3.2 FILLING THE GAPS 5

4. ICE CLASSIFICATION ISSUES 5

4.1 BACKSCATTER CHARACTERISTICS OF ANTARCTIC ICE 6

4.1.1 *Shipborne Scatterometer Signatures* 6

4.1.1.1 The Ice Margin and Pancake Ice Floes 6

4.1.1.2 Nilas 7

4.1.1.3 White Ice Floes 7

4,1.1.4 Smooth First-Year Ice Floes 8

4.1.1.5 Rough First-Year Ice Floes 8

4.1.1.6 Multiyear Ice Floes 9

4.1.2 *Regional Winter C-band Backscatter Variability* 9

4.1.3 *Snapshot Signature Summary* 11

4.2 THE FUTURE OF ICE CLASSIFICATION 13

4.2. I *Scatterometer Ice Classification* 13

4.2.2 *Multi-channel and Multisensory Data Fusion* 14

5. ANTARCTIC SEA-ICE DYNAMICS 14

5.1 LENGTH SCALES OF ANTARCTIC SEA. ICE DRIFT 15

5.1.1 *Coastal Regime* 15

5.1.2 *Central Basin* 15

5.2 MOTION SPECTRA AND TEMPORAL COVARIANCE WITH WIND 16

5.2.1 *Buoys under relatively free drift* 16

5.2.2 Coastal *Shallow-Water Buoy Drift* 17

5.3 LARGE- SCALE SEA-ICE TRACKING USING VISIBLE WAVELENGTH DATA 18

5.4 SMALL-SCALE SEA-ICE TRACKING FROM SAR 18
5.4.1 Perennial Ice Drift 19
5.4.2 Seasonal Ice Drift 19
5.4.3 Sea-Ice Deformation 20

6. ALGORITHM ISSUES 21

6.1 ANTARCTIC ICE-MOTION TRACKING PERFORMANCE 21
6.1.1 SAR motion tracking validation 21
6.1.2 Timeseries Observations of Ice Floes 22
6.2 TEMPORAL CHANGES IN ICE CHARACTERISTICS 23
6.2.1 Summer and Winter SAR backscatter characteristics 24
6.2.2 Timeseries Observations of Backscatter 24
6.2.3 Meltponding 25

7. CONCLUSIONS 25

8. ACKNOWLEDGMENT 27

9. REFERENCES 27

10. FIGURES 31

11. TABLES 33

1. Introduction

Historical data on Antarctic sea ice extent and concentration have traditionally been derived from visible and near-infrared images acquired by the polar-orbiting NOAA meteorological satellites, using the Advanced Very High Resolution Radiometer (AVHRR), and more recently by the Defense Meteorological Satellite Program's Operational LineScan System (OLS) [Massom, 1991]. The limitation of these systems is that the majority of energy imparted to the Antarctic sea-ice system is transferred during frequent episodic storm bursts, caused by fast-moving polar low pressure systems [McPhee *et al.*, 1996]. Since the Southern Ocean sea-ice cover is completely bounded at its lower latitude limit by open ocean, polar-lows transport large amounts of moisture (contained in warm air masses) over the outer ice cover. The result is that most, if not all, noteworthy periods of wind- and temperature-driven dynamic changes in the ice cover are accompanied by periods where the region is blanketed by cloud, and when the atmosphere is inherently more electromagnetically opaque. During storms, the probability with which the area is cloud covered is extremely high, thereby ruling out use of visible or near-infrared images as a practical method of monitoring the associated changes in ice conditions. Instead, Nimbus-7 Scanning Multichannel Microwave Radiometer (SMMR) and DMSP Special Sensor Microwave/Imager (SSM/I) have been the primary workhorses to build up a microwave record of Antarctic sea-ice characteristics. Similar problems, however, occur in passive microwave retrievals of sea-ice concentration, and the algorithms are called into question during these periods of change. Oelke (1996) discovers that the influence of water vapour in the atmosphere alone, can modify the ice concentration retrievals by fractions exceeding 10%, and that retrievals of ice concentration must compensate for the atmospheric water vapour and liquid water contents.

Prior to 1991, the only active microwave radar data to be acquired in the Southern Ocean were collected during the Shuttle Imaging Radar-B (SIR-B) mission of the space shuttle in 1984 (Carsey *et al.*, 1986; Martin *et al.;* 1987). Seasat, in 1978 acquired no Synthetic Aperture Radar (SAR) data due to the lack of a direct broadcast receiving station in Antarctica, and due to the brevity of its lifetime (lasting only 3 months long before a fatal power failure). Despite the brief Arctic success of Seasat, a period of almost 15 years passed before the second radar remote sensing satellite mission was flown. For the first time, the launch of the European ERS- 1 in July 1991 enabled compilation of the first detailed picture of the C-band microwave backscattering characteristics of Southern Ocean sea ice. The launch of an identical ERS-2 in April 1995 provides continuity in this series of Antarctic radar observations.

In this paper, a variety of microwave data sets are presented and the results of these combined data applied in investigations of the spatial and temporal characteristics of sea ice. Since most field data collection and experiments coinciding with the ERS missions occurred within the South Atlantic quadrant of the Southern Ocean, this study focuses particularly upon that Weddell Sea region.

2. **Obtaining Spaceborne Radar Data in Antarctica**

2.1 Antarctic SAR Data

The following sections briefly describe the data from currently operating SAR satellites, which can be received and recorded in Antarctica. Figure 1 shows the present locations of three operational Antarctic receiving stations.

2.1.1 ERS-1 and ERS-2 SAR

Since 1991, the European Space Agency (ESA) ERS- 1 and ERS-2 satellites have acquired microwave radar image data of the Weddell Sea. The C-band imaging SAR mode of the Active Microwave Instrument (AMI) on board ERS allows w-polarized backscatter (o;) data to be collected (i.e. wavelength λ = 5.6 cm). Presently, these are the only operational instruments capable of acquiring high-resolution (approximately 30m), all-weather (day or night), frequent repeat, 100 km-swath Antarctic sea-ice images [Drinkwater, 1995 b]. Neither spacecraft has SAR tape-recording capability and data access is limited to the areas of direct broadcast to existing operational and ESA-approved ERS- 1 Antarctic ground receiving stations [ESA Earthnet, 1992].

2.1.2 J-ERS-1 SAR

Scientific data from the L-band (1.2 GHz) Japanese Earth Resources Satellite (J-ERS-1 - or "Fuyo") SAR have been made available to approved investigators by the National Space Development Agency (NASDA) of Japan. Currently, hh-polarized backscatter (σ^{o}_{hh}) Antarctic data can only be acquired within the Syowa and McMurdo station 'mask' areas shown in Figure 1. These SAR data may be ordered at "research" cost, from RESTEC (Remote Sensing Technology Centre; *i.e. the* distribution agent for NASDA), through a research data distribution and purchase agreement.

2.1.3 Radarsat SAR

The Canadian RADARSAT satellite, launched by NASA on November 4, 1995, carries a C-band hh-polarized SAR. The expected life span of the satellite is five years. Presently, the Canadian Space Agency's (CSA) Radarsat SAR is the only satellite radar offering more than simply 100 x 100 km images. It offers a wide variety of flexible beam modes of which the most unique, the SCANSAR mode, is the only source of wide-swath (500 km) high-resolution (approximately 100 m) ice cover information for the Southern Ocean. However, the only CSA-approved Antarctic receiving station operational and equipped to downlink and record Radarsat data is McMurdo. Radarsat also has on-board tape recorders which will allow a limited amount of data (wide-swath 'narrow' mode) to be recorded and downlinked elsewhere, other than simply at the Antarctic receiving stations. This, in principle, allows data access in any planned location in the Southern Ocean. Until now, no data have been acquired for approved Antarctic investigators. Further information on the Radarsat mission and its operating modes can be found at the Radarsat URL (http: //radarsat.space. gc.ca).

2.1.4 ERS SAR BackScatter Calibration Accuracy

SAR data products received and processed by the German Processing and Archiving Facility (D-PAF) must be treated differently than most US processed ERS data, since they are distributed in a full resolution (i.e. 12.5 m pixel spacing), uncalibrated image form. According to a study by Bally *et al.* (1995) for these 3-look SAR images (i.e. ESA SAR.PRI products), the single pixel (12.5 m) 90% radiometric confidence interval is bounded by a ±4.5 dB interval. Thus, the probability that the measured intensity lies within a ± 4.5 dB error bound is 90%, whereas the radiometric accuracy and stability errors are within specifications of a fraction of a dB (Laur *et al.*, 1993).
To calculate the SAR backscattering coefficient (σ^{o}_{SAR}) of a distributed target which corresponds to an area of sea ice (N pixels in extent), averaging is performed. Block averaging is generally first used to create a speckle-filtered image, with the new equivalent number of looks modified by the area of block averaging together with the target area (i.e. number of pixels averaged from target). The resulting confidence interval for an 8 x 8 block-averaged image with 100 m pixel spacing exceeds 90% for ± 1 dB bounds. With further target averaging of a sample box of over 250 pixels (*i.e.* 16x 16 pixel box), a confidence level exceeding 90% maybe achieved with error bounds of ±0.5 dB. Over 99% probability of errors less than ±0.5 dB maybe reached with samples of greater than 500 pixels (i.e. 23 x 23 pixel box). Thus, for most purposes, having already used a box-filter (8x 8 window) to reduce the image to 100 m pixel spacing, it is generally only necessary to derive samples from target box areas exceeding 8 x 8 pixels to exceed the ±0.5 dB error bound at 99% confidence. All samples presented in this paper are from target areas exceeding this minimum threshold area.

2.2 Antarctic SAR Receiving Stations

It is normally only feasible to acquire high-resolution SAR images within direct broadcast range or line-of-site to a ground receiving station due to the high data rates. Prior to the launch of ERS- 1 in July 1991 there were no satellite receiving stations in Antarctica equipped to downlink or record SAR data. Since 1992, a chain of contiguous SAR-data reception areas has been developed to support the SAR data requirements of a number of nations. Currently, McMurdo (US.), O'Higgins (German) and Syowa (Japanese) are all equipped and capable of downlinking and recording SAR image data. Figure 1 illustrates that almost complete spatial coverage of the mean maximum seasonal ice extent is possible when each of the 3 stations are operating together.

The first SAR station to open in Antarctica was the German Antarctic Receiving Station (GARS) at the Chilean General Bemardo O'Higgins station, located on the northern end of the Antarctic peninsula (at 63.32°S 57.90°W). GARS has been collecting ERS- 1 data since October 1991, but its data reception is limited 1-2 month "campaign-style" operating periods, when manned, Normally these periods typically coincide with German Antarctic experiments, or periods when the German icebreaker R.V. *Polarstern is* operating in the Weddell or Bellingshausen Seas. To-date the O'Higgins receiving station has enabled the most comprehensive SAR data records of Antarctic ice to be collected.

Presently, SAR data are transported out of Antarctica by ship or aircraft (via the Chilean *Teniente Marsh Base),* thereby resulting in delays before SAR image processing takes place. However, a high-speed satellite link is being developed which will (in late 1996) enable McMurdo SAR data to be relayed back to the US for processing at the Alaska SAR Facility (for further information see ASF URL: http: //www.asf.alaska. edu). The recent addition of Radarsat with its tape-recording capacity has increased the flexibility for recovering information in inaccessible locations such as the Southern Oceans.

2.3 Scatterometer Imaging

The non-imaging Wind Scatterometer mode of the AMI on board ERS (EScat) enables continuous radar coverage of Antarctica along a 500 km swath during the period when the SAR is switched off. Low bit-rate EScat data (with an intrinsic resolution of approximately 50 km) do not require direct station transmission and are tape recorded and downlinked to more accessible ESA ground stations [ESA Earthnet, 1992]. Scatterometer σ°_{vv} data can therefore be collected at times and in regions where direct SAR downlink is impossible. Extensive daily coverage of the ERS- 1 scatterometer is particularly valuable due to the lack of data reception in the AMI SAR mode when Antarctic receiving stations are closed, This is especially true in the Weddell Sea, because of the "campaign-style" operation of GARS and limited access to Syowa.

A method is proposed using data acquired in the EScat mode for mapping sea-ice characteristics over the entire Southern Oceans ice cover. Recent advances in image generation from Scatterometer data [Long *et al.,* 1993; Drinkwater *et al.* 1993] enable complementary, medium-scale resolution images to be generated from EScat orbital swath data. This method allows construction of enhanced resolution (approximately 12-14 km) scatterometer images from the backscatter data record, and, by virtue of the wider swath and larger coverage allows mapping of the entire sea-ice cover in a few days [Drinkwater *et al.,* 1993a]. The advantage of EScat image data is that they form an uninterrupted sequence of C-band backscatter of Antarctic sea ice from December 1991 onwards. Not only are these data critically necessary to fill in areas of sparse temporal and spatial radar data coverage, but are also complementary to the restricted incidence angle data (20-26° incidence) of the SAR. The contrasting 20-60° incidence angle diversity of these C-band scatterometer data enables much greater capability for discriminating ice types around Antarctica than either SAR or passive microwave alone. Coupled with higher frequency passive microwave and finer resolution SAR, these data enable a better understanding of the time sequence and seasonal history of Antarctic sea-ice formation, drift, deformation and decay.

3. **Sampling Issues**

3.1 Temporal and Spatial Coverage

One of the priorities for scientific studies of polar ice and snow is high spatial and temporal coverage, due to the short timescales of variability in snow and ice conditions. Exploitation of radar data, particularly in studies related to the mapping and monitoring of the sea-ice cover, was one of

the main driving forces behind inclusion of the SAR instrument on board ERS- 1 [Drinkwater, 1995a]. A large number of sea-ice studies are currently being performed using Arctic Ocean SAR data received at northern hemisphere ground stations the Alaska SAR Facility, Fairbanks (and Gatineau, Canada; Kiruna, Sweden; and Trornso, Norway). Together these SAR receiving stations enable the majority of the northern hemisphere sea-ice cover to be mapped using the SAR, especially at the latitudinal limit of the orbit where the SAR swaths converge. Contrastingly less coverage is possible of the more extensive Antarctica sea-ice cover due to the latitudinal extent of the sea ice and the limited operating times of GARS and Syowa. The result is a high resolution SAR image database which is at best discontinuous in space and time. Alternative methods have therefore been sought using other forms of EScat data, in order to. fill the temporal active microwave record in space and time.

3.2 Filling the Gaps

The key advantage of ERS scatterometer is that it operates whenever the SAR is switched off, continuously retrieving information from the Weddell Sea without the necessity of a local receiving station. Its wider swath provides more frequent, and broader incidence angle ($20° \leq \theta \leq 60°$) coverage in a given location. This low-bit-rate (LBR) data source is essential to fill in areas of sparse temporal and spatial SAR coverage of the Antarctic ice cover, Until now, the intrinsic low resolution of the raw measurement data is the main reason why scatterometer data have not been used in such applications. Nevertheless, the approach described by Drinkwater et *al.* (1993a) produces weekly backscatter maps of the entire Southern Ocean sea-ice cover at a resolution higher (approximately 12 km) than present conventional alternatives such as the SSM/I passive microwave radiometers. EScat images form an uninterrupted sequence of vv-polarized C-band backscatter (σ^{o}_{EScat}) of Antarctic sea ice from the beginning of the ERS- 1 mission. Since these backscatter images are based on multiple azimuth and incidence angle observations, these data provide greater capability for discriminating ice types and separating of ice from ocean. Coupled with higher frequency passive microwave and finer resolution SAR, these data enable a better understanding of the time sequence and seasonal history of Antarctic sea-ice formation, drift, deformation and decay. Furthermore, medium-scale resolution EScat images essentially provide the large-scale context within which the high resolution SAR images maybe interpreted.

4. **Ice Classification Issues**

Recognition of Antarctic sea-ice types in C-band microwave images, as a proxy for ice thickness, is limited by the lack of historical sea-ice signature database equivalent to that existing for the Arctic [Drinkwater, 1995a]. Only since ERS-1 has flown have surface experiments focused on the acquisition of a microwave database for comparison with satellite measurements. These provide the foundation for preliminary attempts to recognize and categorize ice types observed in SAR and Scatterometer images. Due to the logistical constraints of working in accessible regions, most of these measurements have been focused in the Weddell Sea. Results from these demonstrate that Antarctic ice appears considerably different from its Arctic counterpart, due in part to its relatively higher salinity and younger mean age and thickness [Drinkwater e? *al.*, 1993a].

4.1 Backscatter Characteristics of Antarctic Ice

Since the launch of ERS- 1, C-band radar backscatter characteristics of Antarctic sea ice have been investigated during a number of Weddell Sea surface experiments [Drinkwater *et al.*, 1993b; Hosseinmostafa et al., 1995; Drinkwater et *al.*, 1995a; Lytle *et al.*, 1996]. Most, however, have focused on the smaller-scale influences of sea-ice physical properties upon surface-scatterometer measurements, without placing them in the context of satellite radar measurements. In this section, a synthesis is provided of small- and large-scale measurements, using the shipborne track and ERS SAR image locations shown in Figure 2. Examples of field observations and SAR measurements are provided together with corresponding surface validation from the 1992 Winter Weddell Gyre Study (WWGS '92) [Lemke, 1994; Drinkwater and Haas; 1994].

4.1.1 Shipborne Scatterometer Signatures

Field backscatter data were acquired in 1992 using a shipborne microwave radar, during WWGS '92. A C-band (4.3 GHz) frequency-modulated continuous-wave radar scatterometer was operated from the port rail of R.V. *Polarstern* to obtain shipborne measurements of the microwave scattering properties of Antarctic sea ice in mid-winter [Drinkwater *et al.*, 1995a]. The radar had dual polarization, enabling like- (vv) and cross-pol. (hv) data to be acquired at a variety of incidence angles ($15° \leq \theta \leq 700$). When the ship was stationary by a large, uniform ice floe, the instrument was scanned in the vertical plane to obtain σ^{o}_{Ship} independent measurement samples as a function of incidence angle and polarization, In support, detailed surface measurements were made within the footprint of the shipbome radar, after each scan was performed, Surface information comprises snow and ice physical and chemical properties measurements together with structural information [Drinkwater and Haas, 1994]. The objective of the 1992 winter scatterometer measurements was to provide validation data for ERS - 1 SAR observations and to obtain a detailed microwave backscattering catalogue of various ice conditions. Overlapping data acquisitions were planned and made possible by the GARS as part of the International Space Year Project [Lemke, 1994].

4.1.1.1 *The Ice Margin and Pancake Ice Floes*

The Antarctic outer ice margin or marginal ice zone (MIZ) is typically characterized as a high-energy wave environment, where wave propagation into the ice edge plays a dominant role in determining the style of ice formation during winter ice advance, and the characteristics of floes during ice-edge recession. The MIZ is typically broad in its extent during ice-edge advance. In 1992, during WWGS '92, a high amplitude swell was experienced along the Greenwich meridian and frazil and pancake young-ice growth was observed for hundreds of kilometers from the MIZ into the seasonal ice zone. Figure 3a shows a photograph taken in June 1992, of these swell-rocked pancakes in the location of Maud Rise. In contrast, after the peak ~~extent~~ in ice extent the ice edge is X typically in a recessional mode, and the MIZ usually comprises brash ice and a mixture of small wave broken floes and wave-washed piles of rubble.

In contrast to the situation for nilas and young ice forms found in calm environments, pancakes were found to be almost ubiquitous at the ice margin (along the Greenwich meridian), during ice

edge advance in 1992. The occurrence of vast expanses of pancakes and/or streamers with densely-packed sub-resolution floes results in an extremely characteristic marginal ice zone signature [Drinkwater *et al.*, 1993a; Gohin, 1995; Early and Long, *In* Press]. Typically riding on the surface of waves, small wave-washed, porous pans often have a high salinity (Figure 3b) and sufficiently high permittivity that there is relatively strong backscatter near nadir. The rate at which σ^{o}_{Ship} falls with incidence angle, however, appears dependent on the size and packing density of the pancakes, the amount of open water between them, and how wet or deformed their surfaces are. Figure 3b shows the salinity characteristics of a pancake sampled on 13 June, 1992, and Figure 3c contrasts the 13 June radar signature with another site from the following day. The 13 June signature is greater by 10 dB throughout the incidence angle range, with values exceeding -5 dB at 40° incidence or more, due in part to the denser packing of pans, and their rough, deformed and often rafted surfaces. In cases of smaller pancakes spaced by open water, as on 14 June, σ^{o}_{Ship} falls more rapidly. Gohin (1995) reports an intermediate MIZ signature (in his Figure 15) which appears a composite of backscatter curves originating over combinations of open water and dispersed floes, or even low concentration patches of pancakes.

Considerable azimuthal anisotropy is also noted in pancake ice margins in the ERS scatterometer data [Early and Long, *In* Press], and is likely due to the fact that the pancakes damp out smaller gravity and capillary waves, leaving only long wavelength swell waves. This results in a dominant wave-propagation direction sensed by the scatterometer in some circumstances. Future attempts to fit the functional form of the wind relationship may enable wave propagation direction to be derived.

4. 1.1.2 *Nilas*

Large expanses of recently formed nilas (< 10 cm thick) have rarely been observed during surface shipbome experiments, largely because Weddell Sea experiments have focused on the ice margin, and swell-influenced regions of the seasonal ice pack. Consequently, the total fraction of ice formed under calm, non-dynamic conditions is small, and the opportunity to sample large areas other than in recently opened leads or polynyas with scatterometers is rare. Some young ice was observed during WWGS '92, which is reported in Drinkwater and Haas (1994). When observed, nilas typically had little or no snow cover other than frost flowers. The typical signature includes large backscatter coefficients at near nadir angles, with a high gradient of σ^{o}_{Ship}, falling to values less than -20 dB at high incidence angles. A large sample of calibrated SAR pixel values shown in the black probability distribution function in Figure 4 (from all image locations in Figure 2) testifies the likelihood of finding large fractions of new ice and nilas with values below -15 dB is rare in the central Weddell Sea, and extensive nilas areas are generally only found in locations of persistent divergence such as coastal or ice-shelf polynya systems.

4.1.1.3 *White Ice Floes*

The mean thin first-year ice or white ice (in the range 30-50 cm thick) signature shown in Figure 5a, is typical of ice observed in the divergent central Weddell Sea region and is an average of 7 individual site measurements made from 1-14 July, 1992 in the location of scene 5377_5031

(Figure 2). The signature of this relatively smooth, light snow-covered (1-6 cm snowdepth) ice has σ^{o}_{Ship} values between -24 and -26 dB in the ERS SAR incidence angle range $20° \leq \theta \leq 26°$, an intermediate gradient of around 0.49 dB/° from $20 \leq \theta \leq 60°$ incidence, and a neutral cross-polarized backscatter curve. Large expanses of white ice were scoured by strong winds, and had snow depths of less than 5 cm. Lytle *et al. (1996)* have shown previously that snow-free young ice (10-30 cm thick) may result in extremely low backscatter values in an equivalent incidence angle range, thereby increasing as the ice ages (in the absence of deformation) and roughens. These results nevertheless infer that smooth, level white ice with a bare ice surface or shallow snow cover alone do not play a dominant role in driving the backscatter to values shown in the pdf's in Figure 4, and suggest alternatively that areas of congealed pancakes or ridged portions of sea ice drive up measured SAR values in this extensive region.

4.1.1.4 *Smooth First-Year Ice Floes*

The mean signature of smooth, level (undeformed) uniform first-year ice floes of Figure 5b is constructed from 9 individual scatterometer samples, each site of which exceeded 60 cm ice thickness. A distinguishing feature of this signature is that σ^{o}_{Ship} exceeds that of the white ice signature at all angles. The surface roughness of such level ice is generally greater than those white ice forms, while also displaying an older and deeper layered snowcover. ERS SAR backscatter values of equivalent ice floes are expected to fall in the range $-8.8 \leq \sigma^{o}_{Ship} \leq -16$ dB, based on the surface scatterometer measurements, but this is heavily dependent on the physical surface characteristics.

A typical medium thick (67 cm) first-year ice sample acquired on 13 July 1992 at 65.99° S 33.53° W had interleaved bands of frazil and columnar sea-ice crystal growth, and 12 cm of layered snow. The snow-ice interface temperature was -13° C, despite air temperatures lower than -30° C, and an accompanying salinity at the ice surface of 14 psu. Angular depth-hoar crystals developing under the strong thermal gradient in the basal snow, contained significantly more salinity than the ice surface itself, having typical values of around 27 psu. This highly saline, rough scattering interface at the base of the snow, probably accounts for extremely high backscatter values in the range 20-26° in Figure 5b. Likewise, the remainder of the snow contained significant salt content, and airborne spray from nearby leads are thought to be a contributor to the mean background level of surface snow salinity of 2 psu.

4.1.1.5 *Rough First- Year Ice Floes*

Well deformed, ridged or rubbled first-year ice floes are difficult to measure using a shipborne scatterometer, because a complete incidence angle scan is not possible from a fixed viewing position when the local topography is punctuated by piles of ice blocks. Shipborne scatterometer measurements were limited to 5 sites where surface roughness was relatively evenly distributed, and where the signature was not significantly biased by *one* or more features within the scan. The result is the mean signature in Figure 5c. Values of σ^{o}_{Ship} are lower at near normal incidence, and fall between -11.7 and -15 dB for the SAR incidence angle band. The gradient in σ^{o}_{Ship} is approximately -0.52 dB/° in the 20-60° range, but the small sample size and averaging of individual

ridges or local roughness elements cause the variability in measurement points around the logarithmic fit. Cross-polarized backscatter is greater and more variable for these rough ice floes, especially in the *20-40°* range, and is explained by second-order scattering effects such as multiple scattering from blocks.

4.1.1.6 *Multiyear Ice Floes*

According to the field scatterometer data in Figure 5d, multiyear ice floes (largely second-year ice) are practical y indistinguishable from rough first-year ice forms in the ERS incidence angle range. Undeformed, old floes were distinguished on the basis of snow depth, salinity and thickness as second-year ice. Mean net annual thermodynamic ice growth is estimated to be around 1.5 m in the absence of dynamic thickening, based on the lifecycle, mean snow depth and annual net freezing rate in the Weddell Sea [Fischer, 1995]. However, perennial ice floes observed during WWGS '92 comprised massive undeformed ice with considerable snow accumulation. Snow depths exceeding 0.75 m were commonly measured [Massom *et al., In Press]* while ice thickness ranged from around 2 m upwards. Shipborne scatterometer σ^{o}_{Ship} values from these floes fall between -12 and -15.5 dB, and the low gradient of -0.36 dB/° observed in the 30-50' incidence angle range, is caused by snow volume scattering from layers and distinctive ice lenses and ice pipes [Massom *et al., In Press].* To account for the volume scattering characteristics exhibited in Figure 5c, a modified 3rd order polynomial fit is applied instead of a single parameter exponential, to accommodate the flattening at 25° and rolloff beyond 55°. The distinctive plateau and higher backscatter value in the range 40-50° maybe used in 40" incidence EScat images as a method for discriminating high concentrations of thick, snow-covered perennial ice.

4. 1.2 Regional Winter C-band Backscatter Variability

Figure 2 shows a map of the Weddell Sea region, indicating regional locations of several winter SAR image frames (in bold) listed in Table 1. Corresponding image probability distribution functions (pdfs) of calibrated backscatter coefficients are shown in Figure 4. Each pdf comprises individual pixel values from 8 x 8 averaged and calibrated full-resolution SAR.PRI images (originally 8000 x 8000 pixels), thereby resulting in 1 x 10^6 pixel samples per 100x 100 km frame.

A global pdf histogram indicated as the black stepped line in Figure 4 (shown as bar-histogram with 0.1 dB bin width) shows the combined pdf from all images shown in Figure 2, including those listed in Table 1. This summary pdf indicates a tri-modal distribution of backscatter σ^{o}_{SAR}, with distinct components forming peaks at -11.5, -7.5 and -2.5 dB. Individual colored image pdf's indicate that the highest backscatter mode comprises pixels containing glacial ice *(i.e.* ice shelf). Image 5090_512 1, in Figure 2, was acquired in the vicinity of R.V. *Polarstern as* she made a transect along the periphery of the Riiser-Larsen ice shelf. This scene contains a significant number of ice-shelf pixels, falling in the range -5 to +5 dB: air temperatures were around -15° C at the time of SAR imaging. Similar characteristics are observed in the upper peak in the histogram of image 5387_5967. This image captures a large iceberg drifting in the outer marginal ice zone (MIZ), north-east of the tip of the Antarctic peninsula, Its backscatter values exceed those of the ice shelf in the previous example, due in large part to its lower latitude and warmer air temperatures. Glacial

ice, therefore, comprises a distinct portion of the upper limb of the backscatter distribution in the Weddell Sea, and may conveniently be used in winter to find tabular icebergs of significant size, either in the marginal ice zone or within the interior ice pack. Non-tabular Antarctic icebergs do not always present a uniform target area to the SAR, and rotation and drift with respect to the imaging swath often result in a reduction in contrast between the iceberg and its surrounding background.

The next brightest component distribution is described by the pdf of two contiguous image frames (5387_5949 and 5387_5967) along an orbit crossing the Western Weddell Sea MIZ (Figure 2). The peaks in their image histograms overlap almost identically, but for a small transition from the swell-disturbed marginal ice zone to the outer ice edge. Mixtures of brash ice and small first-year ice floes, together with occasional multiyear ice floes characterized the swell-rocked ice margin at the time of SAR imaging [Haas *et al.*, 1992]. Air temperatures and windspeeds at the time of imaging were recorded on board R.V. *Polarstern as* between -5 and 0° C, and 5 and 10 ins-l, respectively. These mixtures have an extremely distinctive signature, with σ^{o}_{SAR} values ranging between -10 and -5 dB, with a mode at -7.3 dB. Rough surface scattering, Occurnng from sub-resolution floes, has a distinctively uniform texture, and bears a close resemblance to wave-disturbed northern hemisphere marginal ice zone ice signatures observed by airborne SAR in the Labrador Sea [Livingston and Drinkwater, 1991; Drinkwater and Squire, 1989]. The further into the marginal ice zone one traverses, the higher the probability of observing large undeformed first-year ice floes and new ice in leads. These pixels appear as a toe of darker material in the histogram of image 5387_5949, extending from -12 dB down to around -19 dB.

Signatures similar to the previous MIZ cases (in terms of backscatter amplitude), may be encountered in the central ice pack, but with the obvious distinction of visible ice-floe outlines. Image 5249_4941, shown in Figure 6 (overlapping the path of R.V. *Polarstern*), contains a typical mixture of perennial and seasonal ice, and was acquired in the outflow path of old ice from the Weddell Sea. The mixture histogram combining these two distinctive end-members appears as a broad pdf in Figure 4. Shipbome observations, noted by Haas *et al.* (1992) as *Polarstern* traversed the region encompassed by this image (less than 24 hours after SAR imaging - see Table 1), indicated a closed ice cover (100% concentration) comprising level first-year ice punctuated by distinct ridges and rougher multiyear ice in fractions up to 30%. First-year ice was extremely rubbled and ridged, particularly around the perimeter of thick multiyear ice floes. The broad pdf, comprises two overlapping distributions without distinctive peaks, due to the continuum of states of the ice ranging from patches of smooth, relatively undeformed first-year ice, to old, deformed snow-covered floes. Individual SAR image samples identified in Figure 6 and tabulated in Table 2 are shown later and used to illustrate the distribution of backscatter in small-scale areas.

The least deformed, or level first-year ice is observed in images 5377.5031 from the central Weddell Gyre region, and 5449_5 139 from the southern Weddell Sea (Belgrano Bank) region (see Figure 2). Both yield distinctive pdf modes between -12 and -13 dB. The former is a largely divergent region, in which vast expanses of undeformed white ice alternated with snow-covered stony fields along the transect of *Polarstern* [Haas *et al.*, 1992]. July air temperatures remained

stable around -27° C and ice formation was almost immediate under divergent conditions. The SAR image indicates no open water, and an extremely low ridge density. The example from the southern Weddell (image 5449_5 139) in contrast contains a larger proportion of deformed seasonal ice (with higher ridging density), and a small fraction of grounded icebergs and perennial ice exiting the basin northwards [Viehoff and Li, 1995]. These higher backscatter components of the scene account for the higher pdf mode for image 5449_5 139 in Figure 4, and the tail extending to values exceeding -5 dB. Based on the predominant drift direction, the origin of the old ice and icebergs found in this region appears to be the Filchner ice shelf front, or the location of grounded icebergs A22 and A23. Large 5-10 km diameter high backscatter (-7 to -2 dB) multiyear ice floes are clearly conglomerates of distinctive old ice floes cemented together by a matrix of what was likely deformed, snow-covered seasonal ice. Floes have broken away and drifted north-westward in the distinctive streamer of bright material [Drinkwater, *In* Press]. Similarly, the iceberg chain described by Viehoff and Li (1995), which originated as one large iceberg from the Filchner ice shelf, subsequent y grounded on the broad GeneraI Belgrano Bank. Ice-motion data obtained from SAR, Scatterometer and buoys provide complementary evidence for this assertion, but further supporting evidence is provided in the form of tracks of deformed sea-ice created as the sea ice drifts past the location of each of these icebergs (see Viehoff and Li, Figure 9). The ice cover had drifted in an extremely constant fashion northwards past the icebergs, leaving linear tracers of deformed material extending 100 km in the direction of drift. At a typical drift speed of 16 ems-l north from the iceberg barrier, these features represent a period of around 1 week. Furthermore, the persistence of such bands (in lee of the icebergs) in time as well as in space ($\geq$100km) indicate a consistent ice drift direction and relatively homogeneous ice motion field in this location.

Examples from images 5377_5031 and 5449..5139 indicate that the least deformed first-year ice generally comprises the leftmost peak in the global pdf (indicated as the black histogram in Figure 4). Old ice and marginal ice on the other hand fill an overlapping range in backscatter to form the central peak in the global pdf. As expected, heavily ridged or deformed first-year ice fall squarely in the middle of the range, and comprise the main peak in image 5090_5121. The roughness of sea ice in the location of this SAR image is further described by laser altimeter flights made from *Polarstern*, with mean ridge heights of the order of 1.2 m and a mean ridge spacing of 54 m [Dierking, 1995]. Therefore, for the central ice pack, linear mixing of the two end members (i) smooth undeformed ice and (ii) thick perennial ice accounts for a continuum of σ^{o}_{SAR} values between -19 and -4 dB. Except for the confusion existing between MY ice and MIZ signatures, the value of SAR backscatter appears closely related to the amount of deformation and ridging density of the ice, or broadly speaking ice thickness. Although backscatter values may be encountered in the range -20 to -25 dB, for newly growing areas of nilas and grey ice (in leads or ice shelf polynya systems), large expanses of such low backscatter material are rarely encountered in the Weddell Sea.

4.13 Snapshot Signature Summary

The SAR image example shown in Figure 6, provides the largest mixture of ice ages and snow depths, due to its prime location in the perennial ice outflow region [Drinkwater, *In* Press]. The

orange pdf in Figure 4 confirms abroad peak comprising a variety of pixels spanning the range of possible white, first-year and multiyear ice σ^{o}_{SAR} values. A number of samples are extracted from this image to generate Table 2. Values describe the signatures of the primary ice components, each of which is extracted on the basis of the scattering characteristics and of their homogeneity. Smooth and rough first-year and multiyear ice mean σ^{o}_{SAR} values range from -16.1 dB to -5.5 dB. In total, a further 60 samples (each of 100 or more pixels) were collected in the same manner from the bold SAR images shown in Figure 2, to generate a summary of snapshot winter backscatter characteristics of these primary ice types. All except the southernmost of the images were acquired in regions in which WWGS '92 surface samples and ice cores were collected [Drinkwater and Haas, 1994]. Figure 7 compares and contrasts the ranges and statistics of these data with matching summary statistics inferred from the mean field scatterometer σ^{o}_{Ship} curves (*i.e.* shaded pdf's) in Figure 5. Additional comparison data is included for open water backscatter coefficients, and MIZ scattering from brash ice or pancakes.

In Figure 7, the MIZ provides one of the largest ranges of backscatter coefficient, due to the influence of floes size, wave environment and variable air temperature. Depending on the season and location, frazil ice growth and pancake formation may be favoured. However, brash ice also provides extremely high σ^{o}_{vv} values due to its similar characteristics in terms of sub-resolution floes and floe packing. A good analogy may be drawn between the Weddell and the Labrador Sea MIZ which was observed by SAR during the LIMEX experiments [Drinkwater, 1989; Livingstone and Drinkwater, 1991]. In Figure 7 SAR and EScat values overlap due to the broad range in scattering conditions described in section 4.1.1.

Field sampling of smooth first-year (FYS) ice floes is inherently biased, since an ice-breaking ship normally seeks the path of least resistance. Although generally true, the route during WWGS '92 was based largely upon large-scale information provided by AVHRR satellite images, and it did not always enable sampling of the smoothest first-year ice. The benefit of SAR images is that they enable the very smoothest ice forms to be easily found and selected. Samples shown in Figure 7 show that the measurement ranges plotted from the shipborne scatterometer and SAR do not overlap particularly well. In other w orals, shipborne radar measurements of smooth first-year ice indicate a higher range of backscatter coefficients than samples selected from the SAR image data. Similarly, the ship navigated around multiyear (MY) ice floes or heavily ridged ice regions visible in the AVHRR images. As a consequence, the multiyear ice which was sampled is at the least deformed extreme of such old ice floes. Haas *et al.* (1992) document the level nature of most of the multiyear ice floes sampled. In particular, σ^{o}_{Ship} values in Figure 7 indicate that the field scatterometer measurements are biased toward the lowermost end of the MY and FYR backscatter ranges.

Other than for smooth first-year ice areas, shipborne scatterometer measurements are generally lower at 40° incidence than equivalent EScat image data extracted in the same locations. Spatial resolution and the averaging over a number of resolution cells influences mean EScat backscatter measurements. Intervening ice motion (typically 1-2 pixels over the 6-day E-scat averaging

window) and resulting mixtures of backscatter elements combine to give a relatively higher σ^0 than that of any individual ice component. In addition, the larger roughness elements dominate the scattering in the higher incidence angle range, yet shipborne scatterometer measurements cannot easily measure the signature of such non-uniform or deformed ice floe surfaces.

Open water signatures are generated in Figure 7 for comparison, using the *CMOD4 algorithm* [Stoffelan *et al.*, 1993]. As expected, the range of backscatter values under differing wind conditions brackets the entire range of sea-ice signatures. Nevertheless, by skillfully using image context (i.e. knowledge regarding the shape of leads within the ice pack) together with ice dynamics information from ice tracking, it is possible to distinguish open water areas within the pack. In any case, the probability of observing an open lead within the Weddell Sea in winter is rare, and for the most part new leads freeze within a matter of hours after opening.

4.2 The Future of Ice Classification

The advent of a global dataset from ERS and NSCAT scatterometers enables uninterrupted C- and Ku-band radar coverage of the Arctic and Antarctic sea-ice cover to be generated. These synoptic-scale images can be exploited to address global ice classification in conjunction with ice dynamics issues. Recent work by Beaven *et al. (1996)* fusing active and passive datasets indicates that radar in combination with SSM/I passive microwave image data increases the amount of independent information and adds dimensionality to the problem of unambiguous identification of classes of ice.

4.2.1 Scatterometer Ice Classification

Early attempts at simple one-dimensional classification of Antarctic ice have used simple supervised clustering analyses on the basis of EScat backscatter statistics. BackScatter coefficients at 40° incidence appear to characterize the large-scale deformation and surface roughness of the sea ice [Drinkwater and Long, 1993]. Simple slicing of an EScat image using the values given in Table 3, yield results shown in Figure 8. Figure 8a is generated for a 6 day period beginning on 16 June, 1992 (day 168), and Figure 8b for a similar period starting at 31 July 1996 (day 213). Each panel in Figure 8 indicates the track of R.V. *Polarstern* during WWGS'92 together with the sea-ice sample sites marked by symbols. Physical descriptions of individual samples of ice are provided by Drinkwater and Haas (1994), together with shipborne scatterometer scattering coefficients (i.e. σ^0_{Ship}).

Figure 8a coincides temporally with the first 4 sea-ice samples acquired along the Greenwich meridian (marked by '+' symbols). The classificat ion routine identifies a large patch of pancake ice formation corresponding directly to the location shown in Figure 3. Table 3 indicates that pixel values highlighted in green fall in the range $-11 \leq \sigma^0_{EScat} < -6$ dB. Later in the WWGS'92 experiment, as *Polarstern* traversed the Weddell Sea, large expanses of undeformed, level white ice were observed ($-20.0 \leq \sigma^0_{EScat} < -14.0$ dB), and the ship track was intentionally modified to avoid a large region of deformed ice (light blue), which was identified in real time using on-board received AVHRR data. Dark blue level first-year ice regions (FYS) are confined at sites marked by 'c)' symbols. The ship track bends around a large patch of deformed, rough first-year (RFY) ice

which originated along the eastern coast of the Weddell Sea and drifted progressively northwestwards from day 168 onwards. The ice outflow region in the northwest Weddell Sea is characterized by rough first-year and multiyear ice (MY) forms, in light blue and green, respectively. In the classified image, the margin between level and thicker, deformed first-year ice closely fits field observations of a boundary between characteristics in first-year ice, where sample sites of thicker, deformed first-year ice are marked by ' O' symbols. At the time of imaging, the ship was preparing to exit the sea ice, in the north-western Weddell Sea MIZ, and 'O' symbols indicate mixed multiyear and brash ice samples in the location of orbit 5387 shown in Figure 2 [Drinkwater and Haas, 1994]. This region of high backscatter corresponds with brash and wave-broken pieces of deformed first-year sea ice and a small concentration of deep snow-covered old ice, and the algorithm classifies the region in green (i.e. pancakes or multiyear ice).

4.2.2 Multi-channel and Multisensory Data Fusion

Further preliminary work to classify sea ice in ERS scatterometer data is being undertaken by Early (unpublished) using isodata clustering algorithms on 3 dimensional ERS- 1 scatterometer image datasets. Three dimensions are constructed from 6-day *A* and *B* images, and an isotropy image, where the primary *A* image is a standard EScat enhanced product, comprising a weekly mean 40° incidence angle normalized backscatter coefficient image. The *B* image is the gradient in scattering coefficient in the 20-60° incidence angle range, and the isotropy image characterizes the azimuthal variance in scattering coefficient and combines information acquired using different beams of the scatterometer instrument.As illustrated by the section above, the main problem in 1 -dimensional ice classification using EScat data is the separation of bright returns from pancake ice, multiyear ice and rough first-year and brash ice. While the former and latter ice type are typically found seasonally in a specific area, it is difficult to unambiguously distinguish perennial ice near the ice margin. The primary advantage of this 3-dimensioned method is that pancakes and brash in the marginal ice zone can be distinguished from multiyear ice in high concentrations. Similarly, rough ice with isotropic scattering characteristics can be distinguished from bright patches of pancake growth, where wave effects create a large degree of anisotropy.

Multi-dimensional algorithms can further address the problems of overlap between the backscatter coefficient distributions by using multi-spectral approaches which merge microwave radar and radiometer data. Beaven *et al. (1996)* and Beaven and Gogineni (1995), for instance, merge SAR and passive microwave data in an attempt to improve sea ice classification. Future studies will attempt to fuse ERS, NSCAT and SSM/I data, to improve ice classifications, especially in situations where atmospheric water vapour limit the accuracy of passive microwave retrievals.

5. **Antarctic Sea-Ice Dynamics**

One of the primary scientific goal of employing high-resolution satellite radar is to generate SAR ice kinematics data products with which to develop a spatial and temporal picture of Antarctic ice drift and opening and closing in response to the momentum transfer [Drinkwater, 1995 b]. The benefit of radar is that it may image the ice night and day, such that a continuous database of images may be

acquired for ice motion tracking processing. Until now, ice-motion studies utilized satellite-tracked buoy data as a means of characterizing the drift and dynamics primarily in the Weddell Sea. AS such, Argos/GPS buoys are also the only source of detailed independent information on ice kinematics. Their drawback on the other hand is that they do not provide information on the spatial characteristics of drift unless they are carefully deployed in a network.

5.1 Length Scales of Antarctic Sea-Ice Drift

Vihma *et al.* (1996) and Kottmeier and Sellmann (1996) have investigated the spatial correlation function of drift in the Weddell Sea using various spatial arrangements of buoy data in 1992. Corresponding length scales are computed from European Centre for Medium Range Weather Forecasting (ECMWF) analysis fields of atmospheric pressure and geostrophic wind. The length scales of sea ice drift and atmosphere appear to vary seasonally and the ice-drift field is especially dependent upon location and primary drift direction with respect to the coast.

5.1.1 Coastal Regime

In the northwards drifting perennial ice regime of the Western Weddell Sea, ice motion is forced by both wind and currents. Periodic deviations from this relatively constant drift pattern are caused by passing cyclones or 'polar lows', Because of the large fractions of thick ice, ice conditions most closely resemble those of the Arctic basin, and thus the ice drift correlation length scales may be expected to vary seasonally and interannually with ice concentration. In 1992, Argos buoys were spaced at intervals in the east-west direction with respect to the Antarctic peninsula, thereby allowing characterization of the east-west correlation functional form. Vihma *et al.* find longitudinal (u_{ice}) and lateral (v_{ice}) integral correlation length scales of 700 and 550 km, respectively. Comparative results of Thorndike (1985) for the Arctic Beaufort Sea are 800 and 600 km, for u_{ice} and v_{ice} respectively. In contrast the east-west integral correlation length scale of the scalar atmospheric pressure was 890 km during this period, while the geostrophic wind integral correlation length scales were u_G = 1050 and v_G = 330 km, respectively. These results indicate that the region of predominantly northward ice motion off the continental shelf exhibits a large decorrelation in velocity in the east-west direction, and that there is confirmed existence of a large gradient in northward velocity components with distance from the Antarctic coast. Indeed, the synoptic pressure pattern also reflects a large gradient in velocity in this same direction.

5.1.2 Central Basin

Kottmeier *et al. (1992)* investigated seasonal and spatial variations in the correlation length and integral length scales of ice motion to find lateral integral correlation length scales ranging between 270-540 km and longitudinal integral correlation length scales of between 490-680 km. Generally, the correlation length scales become smaller with greater mobility of the ice, or vicinity to the ice margin, and the smallest values correspond to summer ice drift near the ice edge in ice concentrations less than 70%. Thus, less compact summer ice tends to have smaller length scales than, for instance, winter ice or ice drifting close to the coastline, as above. In the winter, length scales found by Kottmeier *et al. (1992)* in the central Weddell are somewhat smaller than those

observed in the Western Weddell. Though the basin-scale cumulation in the Weddell and Beau fort Seas is of a similar scale (approximately 1500 km), the difference between these central Weddell length scales and those obtained in the Arctic Basin by Thorndike (1985) suggest that the ice drift differences are caused largely by smaller scales of forcing. Ice motion data derived from satellite radar images must be used to test this hypothesis.

5.2 Motion Spectra and Temporal Covariance with Wind

Ice drift, with respect to previously measured buoy motion in the Antarctic ice cover, 'is known to be highly dependent upon the drifter location with respect to the coast, the primary characteristics of the ocean circulation, and often the water depth. A large distinction can be made between (a) buoys in deep water under relatively free-drift conditions, and (b) buoys drifting in shallow water coastal regimes. The former implies largely divergent situations which characterize the majority of the Antarctic ice cover, and where buoys generally suffer less from internal ice resistance to drift. The latter, in contrast occurs on the continental shelf in situations in which periodic high-frequency tidal currents play a significant role in driving shear motions within the ice cover, and where internal ice stresses can be transferred from the coast to the location of drift during ice convergence events.

5.2.1 Buoys under relatively free drift

Velocity spectra of several freely drifting, deep water buoys in the Weddell Sea are analysed in conjunction with geostrophic wind data to investigate the correlation and spectral relationships between forcing and response. Velocity components of several mid-winter WWGS '92 buoys (with 6 hr resolution data) are computed from 1 month July records in 1992, and concurrent geostrophic wind velocity components estimated from an optimally interpolated pressure field (ECMWF analysis data fitted to weighted buoy pressure measurements).

Figure 9 shows the results spectral analysis of the magnitude of the complex ice and wind velocity vectors. Panels (a) and (b) indicate the temporal autocorrelation functions of this scalar ice and wind speed, respectively, and show a temporal e-folding length scale of less than one day. The cross-covariance function in panel (c) demonstrates clearly that the wind and ice speeds are highly correlated on timescales of $\pm 1d$ and that there is a slight lag of around 12 hours or so between the wind forcing and ice drift response. This confirms that the wind adjusts in a matter of hours to wind forcing, explaining the short response time exhibited by the large-scale ice motion in the example shown later in Figure 11. Similarly, Bartlett filtered power spectra (normalized by the velocity variance) in panels (d) and (e) show clearly that ice drift speed contains the most energy at periods above 100 hours, and the cross amplitude spectrum in (f) shows that the spectra are almost identical in characteristics for this 1 month period. Accompanying coherency and phase spectra of the complex velocities illustrate that the correlation between the wind and ice drift increases rapidly to a peak exceeding 0.8 at periods of 45-70 hours (i.e. 2 - 3 days). This corresponds to the frequency of passing low pressure systems during this winter period, while in contrast the coherency rises to a plateau exceeding 0.8 at periods exceeding 5 days and is comparable to the results of Kottmeier and Sellmann (1996).

The phase spectrum reveals that ice consistently drifts to the right of the geostrophic wind *at all* periods of forcing with respect to the upper level winds, yet with some scatter. July radiosondes launched from R.V. *Polarstern* in the vicinity of the buoy array indicate a relatively constant turning angle of 44° between surface (10 m) and upper level (900 mB) winds (*i.e.* ageostrophic angle of the atmospheric boundary layer). Thus ice drifts with an angle of approximately 25° to the left of the surface wind in this July period. This turning angle is fairly typical of previous results observed by Martinson and Wamser (1990) for drifters in the eastern Weddell Sea in 1986.

5.2.2 Coastal Shallow-Water Buoy Drift

In Figure 10, a comparative correlational analysis is made for the 5 month long drift of Ice Station Weddell (ISW) in the western Weddell Sea in 1992 [ISW Group, 1993], together with hourly winds. IS W was located on an old ice floe just off the continental shelf break at 54° W in the region of perennial ice [Drinkwater, *In* Press]. Its motion in contrast is highly influenced by tidal currents and high-frequency motions. Hourly GPS positions afford the possibility to investigate correlations on shorter timescales than Argos buoys, since the positional errors which accompany hourly interpolated Argos positions are unacceptably large. This limits spectral analysis in Argos buoy data to typically 3 hour or greater sampling intervals, since in practice typically only around 18 to 20 Argos fixes are obtained for each buoy in the Southern Oceans.

This combined hourly GPS and wind record indicates that ice on the continental shelf also responds largely to wind fluctuations on timescales of 120 hours (*i.e.* 5 days) or more. Both the ice and wind auto-spectra indicate a predominant peak at around 500-1000 hours (*i.e.* 20 - 40 days), which represents a dominant response of drift speed to wind fluctuations on timescales associated with synoptically driven pressure systems. Therefore, the monthly mean pressure situation over the Weddell Sea is responsible for the primary forcing of northwards drift in the western limb of the Weddell Gyre. The spectrum for ISW drift speed in Figure 10(g) shows a relatively high degree of coherency for fluctuations of a period exceeding 100 hours, but the phase spectrum indicates a mean of zero (i.e. mean drift along the isobars) with a high degree of variance in the angle between the wind and drift directions for periods up to around 12 hours. This indicates that the ice does not drift in a consistent fashion on short timescales. Short term fluctuations in coherency and phase (below 12 hours) appear to be caused largely by aliasing of motions induced by tidal currents and breakdown of the relationship with wind. Though the geostrophic wind is the predominant forcing mechanism on long timescales, short-term fluctuations in velocity caused by internal ice forces and tides must therefore be considered with respect to satellite observations of ice drift in these regions.

In order to resolve the specific tidal influence, one must focus on non-normalized ice velocity components. Power spectral density results indicate strong diurnal (M_2) and semi-diurnal (K_1 and O,) tidal current forced ice velocity fluctuations, with strong peaks at periods close to 12 and 24 hours. Current meters suspended beneath ISW also demonstrate similar fluctuations (Muench and Gordon, 1996). This result compares favorably with the findings of Viehoff and Li and recent studies of Vihma *et al.* *(1996)* and Kottmeier and Sellmann (1996). It may be expected, therefore, that tidal fluctuations on timescales of 1 day or less have art important impact on the variance in

velocity over the period of satellite repeat orbits. Exact repeat orbits will suffer no serious impact from tidally induced ice-drift velocity variance, whereas image pairs acquired at fractions of, or non multiples of 24 hours, suffer from aliasing of tidally induced velocity components. The impact of tides is discussed in more detail in the context of SAR results later.

5.3 Large-Scale Sea-Ice Tracking Using Visible Wavelength Data

Several remote sensing methods have been used to track sea-ice drift in Antarctica, the most common of which utilizes visible or near-infrared wavelength data, During the WWGS '92 experiment a shipborne HRPT receiving station was used to collect data from the Advanced very High Resolution Radiometer (AVHRR). During this period data from the NOAA-9, NOAA-10, NOAA-1 1 and NOAA-12 satellites were received [Lemke, 1994], Because of missing daylight during the austral winter, overpass information is limited to the infrared channels (3, 4, and 5). Similarly, cloud-free data are relatively sparse. Despite these restrictions, some 170 data sets were recorded throughout this experiment and used for ice motion tracking. Figure 11 shows an example of 3 consecutive ice-motion pairs, from images acquired in June 1992 (10th June: 07:27 GMT and 21:31 GMT; 11 June: 21:07 GMT; and 12 June: 07:51 GMT). These large-scale data [courtesy of the late Thomas Viehoff] indicate that the temporal adjustment to wind forcing is rapid, and especially that the sea-ice drift adjusts to the mesoscale patterns in the wind forcing within a short period of time (and especially in the absence of onshore flow). In Figure 11 this is illustrated by a burst of off ice-shelf winds, which began late on 11 June, which cause a rapid adjustment from predominantly northerly drift conditions to north-westerly drift.

Unfortunately the extent of large-scale examples such as Figure 11 is limited, as is the western extent of the Figure in panels a and b. Together with the restriction of sparse temporal coverage of a given region, this makes AVHRR ice tracking somewhat limited as a source of ice-drift information. This drawback, therefore, is the primary motivation for using microwave data for ice-motion tracking in Antarctica.

5.4 Small-Scale Sea-Ice Tracking from SAR

Recent preliminary studies by Thomas et *al. (1995)* and Viehoff and Li (1995) have used satellite radar data to manually chart regional patterns of ice drift in the Weddell Sea in response to winds and currents. Recent work by Drinkwater and Kottmeier, (1994) introduced ice-motion tracking from mesoscale SAR data as an alternative method for deriving kinematic measurements of the Weddell ice cover. In contrast to the Arctic ice motion studies using ERS SAR [Kwok *et al.*, 1990], the capability to track Antarctic ice using automated SAR motion tracking of had not been demonstrated. The reason was because in the Arctic, large fractions of multiyear ice provide high contrast targets which can be successfully tracked in time using radar images. Weddell Sea ice in comparison exhibits large expanses of low contrast, level first-year ice, and a lack of distinct features with which computer algorithms may successfully track the ice. Here it is demonstrated that SAR images are effective at resolving features which may be used throughout the year in tracking both perennial and seasonal Antarctic ice floes.

5.4.1 Perennial Ice Drift

Perennial ice in the Antarctic shares the some similarities with Arctic multiyear ice, in that it is relatively thicker than its seasonal counterpart, and that it generally supports a high snow load [Massom *et al.*, 1996]. Old ice maybe expected to produce a relatively bright backscatter signature at C-band during all seasons of the year, as demonstrated by examples in section 4.1. During 1992, a series of SAR image acquisitions were planned in conjunction with the drift of Ice Station Weddell (ISW). ISW was deployed on a perennial ice floe in the south-western Weddell Sea [Drinkwater and Lytle, 1996], and positioned over the continental shelf-break at 71.5°S 50"W [ISW Group, 1993].

Figure 12 indicates a result from tracking snow-covered perennial ice floes in the vicinity of ISW during the February - March drift phase of this 1992 experiment. Overlapping image pairs acquired along 1- and 3-day spaced crossing orbits (during the so-called "Ice Phase" orbit of ERS- 1) were correlated to produce ice motion vectors using the algorithm described by Kwok *et al. (1990).* Figure 12 shows the 5 km gridded ice drift displacement field superimposed on the ERS-1 SAR reference image (orbit 3058 frame 5103), acquired at 11:34 GMT on 15 February, 1992 at 71.59° S 53.04° W. Spots indicate the gridded starting positions of tracked features, and the scaled vector arrows indicate the distance traveled in the 17h period separating the pair of tracked SAR images. The location of ISW at the time of the image is indicated by the black symbol '+', and the scaled velocity vector, derived from the corresponding instantaneous GPS locations of ISW, indicated by an arrow. Ice motion vectors around IS W imply strong cyclonic motion, and mean and standard deviations of the u and v velocity components are -10.43±2.5 and 5.95±2.7 cm S-l, respectively. Partial derivatives of velocity over the entire tracked portion of the scene indicate a mean divergence of O. 15± 0.63 % d-', a mean vorticity of -0.45± 0.70 % d-', and mean shear of 2.01*1.02 % d"'.

In total 15 pairs of SAR images were processed to ice drift over ISW, between 7 February and 15 March, 1992 [Drinkwater, In Prep]. Over this period, the mean sea-ice drift speed around ISW was 7.45 ± 1.37 cm s^{-1} on a bearing 323°, while the corresponding mean wind speed was 5.0 m S-l. In summary, there was a net mean divergence of only 0.6% over the period of satellite observations, indicating that net opening of the ice cover was minimal. Indeed both opening and closing events were observed, each effectively redistributing the ice area. Corresponding rotation and shear values were -0.023 ± 0.3* 10^{-6} s^{-1} and 0.65 ± 0.5* 10-6 s-' respectively (i.e. 0.2 ± 2.5% d"' and 5.6 ± 4.3% d-l), indicating shear to be the primary deformation mechanism.

5.4.2 Seasonal Ice Drift

During 1992, several buoys were deployed in the eastern Weddell Sea as part of the WWGS '92 experiment [Lemke *et al., 1994],* in a region comprised of level, undeformed white ice. Simultaneous overlapping SAR acquisitions were planned in July 1992 such that the buoys could be used as validation for the SAR motion retrievals. Under divergent conditions in the Central Weddell Sea, and consequently relatively free drift, the majority of ice drift vectors observed by SAR in the vicinity of the buoy array follow a pattern expected from Ekman dynamics. Figure 13 shows 3-day SAR-observed drift vectors together with the corresponding WWGS'92 buoy drift

tracks marked as dotted Lagrangian trajectories. The superimposed pressure field is optimally interpolated using a polynomial scheme which combines weighted buoy pressure measurements together with 1000 mB ECMWF pressure analysis fields. This technique was originally employed by Kottmeier and Sellmann (1996) but is hybridized here by extending and constraining the fitting procedure to broaden the geographic limits, to include synoptic-scale features and the SAR-tracked domain. Corresponding gridded geostrophic winds are indicated in Figure 13 together with optimally interpolated climatological mean geostrophic currents derived from original data supplied by Ross (Unpublished Thesis) and Kottmeier and Sellmann (1996).

Figure 13a shows a 3-day period with a low pressure system to the south east and relatively constant surface atmospheric pressure conditions over the buoy array (marked by diamonds). ERS-1 SAR ice tracking from two consecutive parallel descending orbits captures the west north-west sea ice drift, which aligns itself approximately along the isobars. The indications are that sea-ice motion in this region can, for the most part, be considered in 'free drift' (Martinson and Wamser, 1990), especially during divergent conditions when ice interaction forces are negligible. As the low pressure system in Figure 13 moved to the east, winds become more southerly, causing increasing divergence as high pressure is reestablished. The weak magnitude of the mean coastal geostrophic current, flowing in the opposite direction in Figure 13a in the location of the buoys, appears to have little impact other than moderating the drift velocity. More deformed coastal ice in SAR drift examples further to the south-east appear to respond more to basal current stresses due to stronger coastal currents which reach 5 cm s-' in magnitude,

Episodic bouts of divergence and convergence are observed primarily in response to storm impulses at the leading and trailing edges of low pressure systems, respectively. Figure 13b shows the mean sympotic and ice-motion situation prior to the example in Figure 13a. In Figure 13b, the passing trough of low pressure causes a rapid adjustment in the buoy drift, each buoy exhibiting a 90° direction change in direction. Geostrophic winds are observed to change from southerlies to westerlies as a consequence of the eastward passage of the low pressure trough, and the SAR motion vectors show a convergence in response to winds towards the Antarctic coast.

During the July drift of the WWGS '92 buoys, the sea ice drifts at a mean Radiosonde balloons launched from R.V. *Polarstern* close to the location of buoy deployment region, show a mean ageostrophic turning angle of around 44° between the upper level and surface winds. The mean angle between the geostrophic wind and the SAR-measured ice drift vectors is observed to vary considerable y in the range ± 20°, depending on the pressure characteristics in the region, as found by Kottmeier and Sellmann (1996). In general, the sea ice in this region drifts to the left of the surface wind vector with a mean turning angle of around 25°, and thus the ice drift vectors for the most part are closely aligned with the isobars.

5.4.3 Sea-Ice Deformation

The advantage which SAR has over large-scale ice motion derived from low resolution satellite images, is that the reformational response of the ice may be characterized. Figure 14 illustrates a

product derived from the SAR ice velocity measurements shown in Figure 12. Ice deformation is graphically described in terms of the ratio of strain-rate invariant E_I and E_{II}, calculated from the velocity derivatives on the 5 km grid-cell scale. The angle of change, θ expresses the style of deformation ($\theta = \tan^{-1} E_{II}/E_I$), where E_I quantifies positive divergence (or negative convergence) and E_{II} the rate of shearing. The result is a graphical illustration of whether the motion is accompanied by either predominantly divergence (i.e. $\theta \approx$ O), shear ($\theta \approx$ 900), or convergence ($\theta \approx$ 1800). We note for the field of cyclonic motion recorded in Figure 12, that a large proportion of the deformation represents shear-style motion (indicated by dark blue and pink). Only one single purple 5 km grid cell located to the north-west of the ice camp (marked by '+') illustrates a situation tending to pure convergence. It clearly begins as an area with a large fraction of open water. Such sea-ice deformation data are presently used in validating ice theologies presently employed in coupled ice-ocean-atmosphere models [Stem *et al.*, 1995].

6. **Algorithm Issues**

Various difficulties in implementing algorithms using Antarctic radar data, may be anticipated on the basis of experience with problems encountered in Arctic applications. The performance of existing algorithms must be tested in the Antarctic, in order to evaluate their skill and accuracy. To date, the main area in which existing algorithms have been tested is ice tracking. Examples are shown here which evaluate the precision and accuracy of ice tracking in Antarctica. Various other scenarios which warrant further study are also briefly illustrated in subsequent sections.

6.1 Antarctic Ice-Motion Tracking Performance

6.1.1 SAR motion tracking validation

Further work to quantify the accuracy of automated sea-ice tracking algorithms used on SAR image pairs has recently been undertaken by DrinkWater (In Prep). Positions of Argos drifter and GPS receivers in the vicinity of IS W are compared with SAR ice-tracked motion vector information to establish the success of algorithms developed for the winter Arctic [Kwok et *al.*, 1990]. The period of consecutive ERS- 1 SAR imaging of the IS W camp floe lasted between day 38 (7 Feb.) through day 75 (15 Mar), in 1992. Results, such as those shown in Figure 12 and 13, demonstrate that algorithms originally developed for the winter Arctic can be used without serious problems in both cases of ISW summer perennial ice or relatively featureless smooth Weddell Sea winter first-year ice. In order to establish the accuracy of the tracking algorithms, however, positions from a fixed GPS receiver at the ISW camp are compared with SAR ice-tracked drift vectors. GPS positional fixes were not logged until after day 57, preventing accurate interpolation of latitude and longitude positions of the camp earlier than this date. The period of highest frequency GPS measurements overlaps with 6 consecutive SAR ice velocity image "pairs" (i.e. 12 consecutive images), allowing comparisons to be made between day 57 and 75. Figure 15 shows the correlation between mean velocity components derived from SAR (such as that in Figure 12) and those derived from instantaneous GPS IS W locations (interpolated to the SAR imaging times). SAR-derived u and v velocity components are rotated into the local coordinate system to match calculated GPS velocities,

In terms of different mean ice drift speeds Figure 15 indicates a sample ranging from 2-10 cm S-l. Figure 15a shows the west-east (*i.e.* x or u component) and 15b south-north (i.e. y or v) components of velocity, while 15c indicates the magnitude of the velocity. Ice drift is largely westward and northward during this period. Though a small sample, the plot shows a high degree of accuracy in deriving both the direction and magnitude of ice drift. Although spatial mean SAR velocities are used in the regression analysis, as opposed to values of the SAR-derived velocity interpolated to the ISW floe location, the result in 15c indicates a correlation of 0.98 (illustrated by the dotted regression line). The rms error in SAR motion tracking is computed to be less than 0.5 cm S-l for 3-day motion tracking. This translates into an error of approximately 100 m, or equivalently approximately 1 pixel after accounting for error variance generated by temporal interpolation of GPS locations and spatially averaged mean SAR velocity vectors.

The largest outlying vector in Figure 15 is identified throughout by a curly arrow, indicating that the motion field displays a large amount of rotation or vorticity. As Figure 12 shows, the mean velocity components of such a field are not sufficiently representative of any single point in space for a good comparison to be made. On the other hand, it is felt that spatial interpolation of velocity field is unrepresentative of true inter-floe motions, and so further attempts are not made to try to improve this comparison.

6.1.2 Timeseries Observations of Ice Floes

Results of processing all 3-day or 1-day repeat overlapping "pairs" into ice kinematics information are shown as a velocity timeseries in Figure 16 together with surface wind speed and the GPS monitored drift of the IS W camp floe. In Figure 16(a) IS W measurements of the wind speed are shown as a dotted line. Prior to completion of the meteorological mast on day 57 once or twice daily windspeeds were recorded. The 3-day smoothed solid line indicates Finnish Salargos buoy (no, 5908) wind speed measurements prior to day 57 (courtesy Timo Vihma), whereafter the solid line is a 3-day running mean of the hourly means recorded by the ISW met station anemometer.

Figure 16 (b) and (c) show the mean SAR instantaneous velocity components joined by a dotted trend line. Horizontal bars indicate the period separating the tracked image pair, and the vertical bar indicates one standard deviation (10) about the mean velocity vector (spatially averaged over a 100 x 100 km scene). An overlapping solid line indicates the 3-day smoothed velocity of ISW and begins upon installation of a fully functional GPS receiver at ISW (on day 57). Hollow diamond symbols represent the velocity computed from distances traveled between instantaneous GPS locational "fixes", at SAR imaging times. Where diamonds overlap mean SAR velocity measurements, the spatially averaged SAR velocity is representative of a single GPS velocity vector. In a spatial context, where the mesoscale velocity field does not represent translational motion, the ISW GPS velocity diamond does not overlap the mean SAR velocity. Thus, in the case of day 70 the discrepancy shown in Figure 16(b) and (c) is explained by strong anticyclonic or cyclonic motion, and is similar to the example in Figure 12. A mean velocity of a spatial field of cyclonic or anticyclonic flow is unrepresentative of any single vector within that field, and such

spatial means cannot be directly compared to the 'ensemble-averaged' IS W GPS-derived velocity. Nevertheless, smoothed 3-day velocity components indicate responses to sustained bursts of wind shown in the solid line in Figure 16(a). Additionally, though not in 'free-drift', SAR-reported drift velocity components (dotted line in (b) and (c)) clearly respond to the 3-day filtered wind forcing. The largest discrepancy between SAR velocity and 3-day smoothed ISW velocity occurs as a result of the wind burst from day 63 to 67, when IS W is pushed to the west at -15 ems-i. In the corresponding SAR image record, the closest pair of image acquisitions was 6-days, and thus the minimum in ISW u velocity (solid line) is missed. A higher temporal resolution in SAR imaging is required to capture such deviations in ice motion.

Generally, examples such as Figure 16 indicate that the sea-ice drift field adjusts to the wind. The temporal frequency of fluctuations in the field of ice velocity vectors closely match those in wind velocity. Temporal sampling of 3-d or less is concluded necessary if the small-scale response to synoptic storms is to be studied in more detail in an open basin such as the Weddell Sea. The shorter timescale examples such as the 1-day repeat orbits plotted at day 46, 52, and 71 capture more variance in ice velocity (indicated by the vertical bars for u and v velocity components). Spectral results in buoy data in Section 5.2.2 confirm this phenomena to be attributable to the aliasing of velocity components induced by tidal motions. Importantly, therefore, exact 3-day repeat orbits do not alias diurnal or semi-diurnal (which are close to 12 hr. period) tidal motions, whereas non-multiples of 12 hours contain significant tidal variance in this location. Ultimately, a trade-off is ultimately necessary between resolution in temporal sampling and the sampling interval over which ice floes are tracked, The best solution appears to be 3-day SAR ice-motion tracking at regular, exact one-day intervals, but issues such as the SAR data volumes (for required coverage of the entire Weddell Sea) become paramount. Radarsat ScanSAR image coverage may be the only future high-resolution SAR solution which can approach this sampling requirement.

6.2 Temporal Changes in Ice Characteristics

The majority of algorithm problems occur as a consequence of large temporal variations in ice characteristics. Timeseries of ERS microwave radar data demonstrate that within ice class backscatter signatures vary both seasonally and interannually in the Weddell Sea. The primary distinction, therefore, between seasonal and perennial ice covers can only be made by separating data acquired during the winter ice maximum and austral summer minimum, or alternatively by continuously tracking perennial ice floes identified during the summer months, through time and space. During February and March of 1992, planned SAR acquisitions over ISW resulted in over 35 calibrated images over this perennial ice zone region. Other, previously described winter SAR data acquisitions were planned during WWGS '92 in locations where R.V. *Polarstern* was traveling across the Weddell Sea, and in a number of additional instrumented locations. The result in 1992 is a total collection of more than 50 images (exceeding 3.5×10^9 pixels) in regions where sea-ice cover was either measured or for which independent sources of information are available. Two examples of seasonal backscatter variability are illustrated below. In the first, all ERS- 1 SAR images in winter and summer states are separated and grouped, and their backscatter statistics

plotted in Figure 17. In the second, in Figure 18, follow a number of ice parcels in space, to illustrate the progression in ice signatures [after Drinkwater and Lytle, 1996].

6.2.1 Summer and Winter SAR backscatter characteristics

If contrasts in mid-winter and mid-summer conditions are first considered, then a collection of all statistics of calibrated backscatter images may be made on the basis of the ice growth or melt seasons. Since the Weddell Sea ice cover is largely composed of seasonal ice, the residual ice cover at the end of summer typifies the various states of perennial ice, all ice surviving the summer melt being defined as multiyear ice. All the grouped pixel values are combined into either summer and winter pdf's in Figure 17 to describe the differences between the summer and winter perennial or annual ice signatures, respectively. The summer pdf shows a mode around -6 dB, with a small tail to higher values comprising highly deformed ice and icebergs. Ice concentrations typically exceeded 95% in the perennial ice pack and the contribution from wind-roughened open water is negligible [Drinkwater and Lytle, 1996]. At the lower end of the summer pdf is a longer tail extending to -15 dB and beyond. This includes level, undeformed multiyear ice, and snow-covered first-year ice thick enough to survive the summer melt.

In winter, the pdf becomes hi-modal with the appearance of seasonal ice. As time progresses, advection of an increasing fraction of multiyear ice northwards out of the basin reduces the probability of multiyear ice, thereby producing the imbalanced bimodal mid-winter distribution shown in Figure 17. While a secondary peak remains, with a mode at around -7 dB, the main peak now occurs at around -12.5 dB and comprises more prevalent forms of level, fret-year ice. The low end of the pdf, at values of -15 dB and below indicate the least deformed fret-year ice. A winter tait extending down to the noise-floor of the SAR (approximately -25 dB) includes very small proportions of new and young ice forms, and recent results from Jeffries and Morris (*Pers. Comm.*) in the Bellingshausen Sea indicate that typical undeformed new ice appears with a mean backscatter value of -23 ± 0.5 dB in small areas of coastal polynyas and flaw leads.

6.2.2 Timeseries Observations of Backscatter

Early observations of the temporally changing C-band backscatter response within fixed regions have been made in Drinkwater *et al.* (1993b). However, temporal monitoring of the backscatter signature of moving floes has not previously been attempted. Studies focusing specifically on multiyear ice in summer and winter SAR images show that its backscatter coefficient changes seasonally, and the mode of the multiyear ice pdf in Figure 17 is observed to shift slightly from around -6 dB to -7 dB between warm and cold seasons (i.e. around 25% change in image scattering intensity). Surface measurements made at ISW [Lytle and Ackley, 1996] illustrate that perennial ice retains a deep snowcover on its surface. A large proportion of the ISW camp floe and surrounding ice floes experienced summer flooding at the base of the snow.

Figure 18 illustrates the temporal change of the SAR backscatter signature of tracked perennial ice floes in the vicinity of ISW as they cooled during the summer-autumn transition period. As the cold wave (i.e. 0° C isotherm) propagates downwards through the snow, areas of flooded or saturated

including ice kinematics fields and area flux information, with which to address mass- or freshwater balance questions in the Southern Ocean.

The most promising application of radar data in Antarctica is undoubtedly the ability to observe ice dynamics in time-sequential datasets. Further work to realize automated algorithms for processing these images to large-scale ice kinematics products will be undertaken in the near future, such that these datasets become widely available to more general users of dynamical information. Ice drift statistics alone are an important advance in understanding how the wind-aided advection of ice influences regional heat and freshwater budgets of the Southern Ocean.

Observation and recognition of particular ice characteristics and types is critical to the interpretation and evaluation of new microwave image products in Antarctica. This paper provides the first broad picture of the backscatter characteristics or "signatures" observed by C-band satellite radars, and serves as a foundation for a catalogue of Southern Ocean sea-ice signatures for regions in which *in-situ* measurements are frequently made. Examples illustrated in this study indicate that Antarctic ice may often look considerably different from its Arctic counterpart, warranting future studies to expand knowledge of its regional and seasonal variability. A caveat is added, however, with relationship to the utility of more general automated ice-classification schemes in Antarctica, especially in regions and seasons where products can not be characterised in terms of their uncertainty. Indeed, the concept and requirement for proxy classes of ice thickness should be revisited, and future algorithms to classify Antarctic ice should be carefully crafted. Future schemes should utilize the present framework of large-scale measurements by passive microwave and scatterometers, together with drawing upon quantitative information derived from direct obervat ions of the kinematics measurements. Together these information sources provide the basis for a more valuable geophysical product than simply ice-type classification.

Coupled regional ocean-ice-atmosphere models will initially benefit from Southern Ocean radar data through more accurate parameterisations of the ice rheology and resulting motion and deformation fields. In turn, they will be used to evaluate the direct relationships between the changing basin-wide distribution of sea ice and the flux of momentum. Accurate monitoring of Southern Ocean ice formation, drift, deformation and divergence is of additional importance to indirect estimation of surface fluxes of heat, freshwater and salt.

Mesoscale coverage of ERS-1 and NSCAT can now be used together with the meteorological and oceanographic data to generate regional surface flux estimates in varying locations in the Southern Ocean, These are presently being compared with the regional distribution of warm and cold water regimes observed in oceanographic data, to map the spatial arrangement of ice surface flux environments with relation to the ocean and atmospheric circulation patterns. Resultant estimates will be compared with simulated fluxes in one and two dimensional coupled sea-ice models to provide keys to the principal sea-ice factors regulating the surface fluxes in ice-covered regions. Furthermore, the advantage of the coverage which the Scatterometer image data provide is to facilitate investigations of links between the Antarctic circumpolar wave and temporally varying

basal snow (slush) cooi and refreeze. In response to this process, C-band microwave backscatter values shown in Figure 18 decrease [after Drinkwater and Lytle, *In* Press]. The period of cooling air temperatures at ISW (Figure 18a) is shown in parallel to thermistor profiles at a variety of sites with differing snow depth (Figure 18b). Thermistors indicate that protracted cold air temperatures after day 63 enable the snow layer to develop a strong thermal gradient. This cools the basal snow sufficiently quickly that the slush freezes around day 67.

Large numbers of individual multiyear ice floes were tracked in ERS- 1 SAR images to derive the microwave backscatter trend shown in the upper trace of Figure 18c. For comparison, global mean SAR-image and EScat-image σ^o_{vv} values measured over the identical 100 x 100km SAR-imaged areas, each report essentially the same decreasing trend. The largest decrease in σ^o_{vv} is observed before and after the freeze-up of the slush. Thus, the change from rough surface scattering from snow-covered slush to rough surface scattering from dry snow-covered perennial ice appears responsible for the observed shift in the multiyear ice peak in Figure 17.

6.2.3 Melt-pending

Additional effects of seasonal melting and transformation at the surface of perennial ice floes are noted here as a consequence of summer processes and periodic winter excursions in air temperature, due to storm systems. Large warm excursions in air temperature have been observed to have considerable impact upon the microwave backscattering characteristics of sea ice, in response to the changing surface snow and ice characteristics [Drinkwater et *al.*, 1995; Massom *et al.*, In Press]. Though the appearance of classical meltponds in the Weddell Sea appears to be checked largely by cold dry southerly winds and the latitude or extent of the southward wandering of the zero degree seasonal isotherm, a recent summer experiment in 1995 recorded surface meltponding in the Weddell Sea [Low, unpublished thesis]. The appearance and expression of meltponding in SAR images is discussed in more detail by Low and Wadhams (In Press) by use of coincident SAR and aerial photography. Ongoing studies of the spatio-temporal expression of seasonal melt in the EScat image timeseries (1992-present day) will reveal the context of these SAR-observed features in the long-term record. Furthermore, these studies are expected to confirm whether extreme melt events noted in 1992 and 1995 are associated with climatic anomolies such as the 4 year period in sea-surface temperature and reduced poleward wind stress observed by White and Petersen (1996).

7. Conclusions

ERS satellite data have for the first time been extensively studied and applied in studies of sea-ice dynamics and characteristics in Antarctica. The main result of analysis of these data is an understanding of how microwave signatures and their time-varying properties can be used as a basis for understanding geophysical changes in the Antarctic sea-ice cover. Examples show that satellite radar is a valuable addition to the arsenal of tools now available for building up the long-term observational database necessary for addressing climate-related issues. Furthermore, algorithms which have been applied to these data will be refined and ultimately lead to data products

attributes of the sea-ice cover. For the first time, high resolution global coverage of sea ice enables teleconnections between mid- and high-latitude processes to be studied in Antarctica in a consistent fashion.

8. Acknowledgment

ERS-1 data were supplied as part of the European Space Agency supportedA02.USA.119 project. Enhanced resolution ERS-1 scatterometer data were processed by David Long and David Early of BYU for this work, as part of a collaborative project. SAR data are processed and supplied by the German Processing and Archiving Facility (D-PAF), and especial thanks go to Jorg Gredel and Birgit Schättler for their product support and Klaus Reiniger for GARS receiving-station support. WWGS '92 buoy data were kindly supplied by Christoph Kottmeier as part of an ongoing collaborative analysis project and Timo Vihma is thanked for use of the Salargos buoy data. Mark Drinkwater performed this work at the Jet Propulsion Laboratory, California Institute of Technology under contract to NASA, with the support of Robert H. Thomas of Code YSG, NASA.

9. References

Bally, P., K. Fellah, Evaluation of the Accuracy of the Backscattering Coefficient Measurement in SAR Data Products, *ESA/ESTEC Earth Sciences Division Technical Note,* July 1995.

Beaven, S., S.P. Gogineni, and F.D. Carsey, Fusion of Satellite Active and Passive Microwave Data for Sea Ice Type Concentration Estimates, *IEEE Trans. Geosci. and Rem. Sens., 34, 5,* 1172-1183, 1996.

Beaven, S., and S.P. Gogineni, Effect of Summer-to-Fall Transition on ERS-1 SAR and SSMA Images of Sea Ice, *Proc. IGARSS '95,2,* Florence, Italy, 10-14 July, IEEE Cat. No. 95 CH35770, 634-637, 1995.

Carsey, F. D., B. Holt, S. Martin, L. McNutt, D.A. Rothrock, V.A. Squire, and W.F. Weeks, Weddell-Scotia Sea marginal ice zone observations from space, October 1984, *J. Geophys. Res.,* 91, C3, 3920-3924, 1986,

Comiso, J. C., T.C. Grenfell, M. Lange, A.W. Lohanick, R.K. Moore, and P. Wadhams. Microwave remote sensing of the Southern Ocean ice cover, In *Microwave Remote Sensing of Sea Ice,* (Ed.) F.D. Carsey, AGU *Geophysical Monograph 28,* Chapter 12,244-259, 1992.

Dierking, W., Laser profiling of the ice surface topography during the Winter Weddell *Gyre* Study 1992, *J. Geophys. Res.,* 100, C3, 4807-4820, 1995

Drinkwater, M.R., The Drift of Ice Station Weddell, In Preparation.

Drinkwater, M.R., Active Microwave Radar Observations of Weddell Sea Ice, *Antarctic Research Series,* American Geophysical Union, In Press.

Drinkwater, M. R., Airborne And Satellite SAR Investigations Of Sea-Ice Surface Characteristics. In *Oceanographic Applications of Remote Sensing,* (Ed's) Ikeda, M. and Dobson, F., Chapt. 21., CRC Press, 345-364, 1995a.

Drinkwater, M. R., Applications Of SAR Measurements In Ocean-Ice-Atmosphere Interaction Studies. In *Oceanographic Applications of Remote Sensing,* (Ed's) Ikeda, M. and Dobson, F., Chapt. 24, CRC Press, 391-406, 1995b.

Drinkwater, M. R., LIMEX '87 Ice surface characteristics; implications for C-band SAR backscatter signatures. *IEEE Transactions on Geoscience arid Remote Sensing , 27, 5,* 501-513, 1989.

Drinkwater, M.R., and C. Kottmeier, Satellite Microwave Radar- and Buoy-tracked Ice Motion in the Weddell Sea during WWGS'92. *Proc. IGARSS '94,* 1, 153-155, Pasadena, CA, Aug. 8-12, IEEE Cat, No. 94CH3378-7, 1994.

Drinkwater, M. R., and C. Haas, Snow, Sea-Ice and Radar Observations during ANT X/4: Summary Data Report, *Berichte aus dem Fachbereich Physik, 53,* Alfred Wegener Institut fiir Polar- und Meeresforschung, Bremerhaven, Germany, 58 pp., 1994.

Drinkwater, M. R., and Squire, V. A., C-band SAR observations of marginal ice zone rheology in the Labrador Sea. *IEEE Transactions on Geoscience and Remote Sensing, 27,5,522-534,* 1989.

Drinkwater, M.R, R. Hosseinmostafa, and S.P. Gogineni, C-band Backscatter Measurements of Winter Sea Ice in the Weddell Sea, Antarctica, *Int. J. Remote Sensing, 16, 17,3365-3389,* 1995a.

Drinkwater, M. R., H. Fischer, M. Kreyscher, and M. Harder, Comparison of Seasonal Sea-Ice Model Results with Satellite Microwave Data in the Weddell Sea, *Proc. IGARSS '95,* 1, Florence, Italy, 10-14 July, IEEE Cat. No. 95CH35770, 357-359, 1995b.

Drinkwater, M. R., D.S. Early and D.G. Long, ERS- 1 Investigations of Southern Ocean Sea-ice Geophysics using Combined Scatterometer and SAR Images. *Proc. IGARSS '94,* 1, 165-168, Pasadena, CA, Aug. 8-12, IEEE Cat. No. 94CH3378-7, 1994.

Drinkwater, M. R., D.G. Long, and D.S. Early, Enhanced Resolution Scatterometer Imaging of Southern Ocean Sea Ice, *ESA Journal, 17,307-322,* 1993a.

Drinkwater, M. R., Hosseinmostafa, R., and W. Dierking C-band Microwave Backscatter of Sea Ice in the Weddell Sea during the Winter of 1992. *Proc. IGARSS '93,* Tokyo, Japan, Aug. 18-21, 2,446-448, 1993b.

Early, D. S., and D.G. Long, Azimuth Modulation of C-band Scatterometer σ^o Over Southern Ocean Sea Ice, Accepted for Publication in *IEEE Transactions on Geoscience and Remote Sensing, 1996.*

ESA Earthnet, ERS- 1 System, *ESA Special Publication,* SP- 1146, ESA Publications Division, ESTEC, Noordwijk, The Netherlands, 1992.

Fischer, H., Comparison of an optimised dynamic-thermodynamic sea-ice model with observations in the Weddell Sea, *Reports on Polar Research,* 166, Alfred-Wegener-Institut fiir Polar- und Meeresforschung, Bremerhaven, Germany, 1995.

Gohin, F., Some Active and Passive Microwave Signatures of Antarctic Sea Ice from Mid-Winter to Spring 1991, *Int. J. Remote Sens.,* 16, 11, 2031-2054.

Haas, C., T. Viehoff, and H. Eicken, Sea Ice Conditions during the Winter Weddell Gyre Study 1992 ANT X14 with R/V *Polarstern*: Shipboard Observations and AVHRR imagery, *A WI Berichte aus dem Fachbereich Physik, 34,* Alfred Wegener Institut für Polar- and Meeresforschung, Dec. 1992.

Hosseinmostafa, A. R., V.I. Lytle, K.C. Jezek, S.P. Gogineni, S.F. Ackley, and R.K. Moore, Comparison of radar backscatter from Antarctic and Arctic sea ice, *Electromag. Wave Applications, 9,421-438, 1995.*

Ice Station Weddell Group, Weddell Sea Exploration from Ice Station, *EOS,* 74, 11, 121 and 124-126, 1993.

Kottmeier, C., and L. Sellmann, Atmospheric and Oceanic Forcing of Weddell Sea Ice Motion, *J. Geophys. Res.,* 101, C9, 20809-20824, 1996.

Kottmeier, C., J. Olf, W. Frieden, and R. Roth, Wind Forcing and Ice Motion in the Weddell Sea Region, *J. Geophys. Res.,* **97, D18, 20373-20383, 1992.**

Kwok, R., J.C. Curlander, R. McConnell, and S.S. Pang, An ice-motion tracking system at the Alaska SAR Facility, *IEEE J. Oceanic Eng.*, OE-15, 1,44-54, 1990.

Laur, H., P.J. Meadows, J.I. Sanchez, and E. Dwyer, ERS- 1 SAR Radiometric Calibration, Proc. of the CEOS SAR Calibration Workshop, ESTEC, Noordwijk, Netherlands, *ESA Pub, WPP-048, 257-281, 1993.*

Lemke, P. (Ed.), The Expedition ANTARKTIS X/4 of R.V."*Polarstern*" in 1992, *Reports on Polar Research,* 140, Alfred-Wegener-Institut für **Polar- und Meeresforschung, Bremerhaven, Germany, 1994.**

Livingstone, C. E., and M. R. Drinkwater, Springtime C-band SAR backscatter signatures of Labrador Sea marginal ice: measurements vs modelling predictions. *IEEE Trans. Geosci. and Remote Sensing, 29,* 1,29-41, 1991.

Long, D. G., P.J. Hardin, and P.T. Whiting. Resolution Enhancement of Spaceborne Scatterometer Data. *IEEE Trans. Geosci. Remote Sensing, 31,3,700-715,* 1993.

Low, D., The Validation of ERS- 1 Summer SAR Data for Antarctic Summer Sea Ice, *Unpublished M.* SC. *Thesis,* 1995.

Lytle, V., and S. Ackley, Heat Flux through Sea Ice in the Western Weddell Sea: Convective and Conductive Transfer Processes, *J. Geophys. Res.*, 101, C4, 8853-8868, 1996.

Lytle, V. I., K.C. Jezek, S.P. Gogineni, and A.R. Hosseinmostafa, Field Observations of Microwave Backscatter from Weddell Sea Ice, *Int. J. Remote. Sens.*, *17,* 1, 167-180, 1996.

McPhee, M. G., S.F. Ackley, P. Guest, B.A. Huber, D.G. Martinson, J.H. Morison, R.D. Muench, L. Padman, and T.P. Stanton, The Antarctic Zone Flux Experiment, *Bull Am. Met, Sot., 77, 6, 1221-1232, 1996.*

Martin, S., B. Holt, D.J. Cavalieri, and V. Squire, Shuttle imaging radar B (SIR-B) Weddell Sea ice observations: a comparison of SIR-B and scanning multichannel microwave radiometer sea ice concentrations, *J. Geophys. Res.,* 92, C7, 7173-7179, 1987.

Massom, R. A., *Satellite Remote Sensing of Polar Regions, Lewis* Publishers, Boca Raton FL, 1991.

Massom, M., M.R. Drinkwater and C. Haas, Spatial and Temporal Distribution of Winter Snowcover Properties on Sea Ice in the Weddell Sea, *J. Geophys. Res.,* In Press.

Muench, RD, and A.L. Gordon, Circulation and Transport of Water along the western Weddell Sea, *J. Geophys. Res.*, 100, **C9, 18503,18515, 1995.**

Morris, K. and M. O. Jeffries, Sea ice characteristics and seasonal variability of ERS-1 SAR backscatter in the Bellingshausen Sea, *Antarctic* Research Series, American Geophysical Union, In Press.

Oelke, C., Atmospheric signatures in sea-ice concentration estimates from passive microwaves: modelled and observed, *Int. J. Remote Sens.*, In Press.

Ross, H., Ein Massenerhaltendes Hydrographisches Inversmodell mit Verallgemeinerter Vertikalkoordinate Angewandt auf den Atlantischen Sektor des Südlichen Ozeans, *Unpublished Ph.D. Thesis,* Alfred Wegener Institut, In Press.

Stem, H. L., D.A. Rothrock, and R. Kwok, Open Water Production in Arctic sea ice: Satellite measurements and model parameterizations, *J. Geophys. Res.,* 100, C 10, 20601.-20612, 1995.

Stoffelan, A., and D.L.T. Anderson, ERS-1 Scatterometer Data Characteristics and Wind Retrieval Skill, Space at the Service of Our Environment, *Proc. 1st ERS-1 Symp., 4-6 Nov. 1992,* Cannes, France, *ESA SP-359,* 1,41-47, 1993.

Thomas, J. P., J. Turner, T.A. Lachlan-Cope, and G. Corcoran, High resolution observations of Weddell Sea surface currents using SAR sea-ice motion vectors, *Int. J. Remote Sensing, 16,* 17, 3409-3425, 1995

Thorndike, A. S., Kinematics of Sea Ice, *The Geophysics of Sea Ice,* (Ed.) N. Untersteiner, 489-549, Plenum, New York, 1985.

Viehoff, T., and A. Li, Iceberg Observations and estimation of submarine ridges in the western Weddell Sea, *Int. J. Remote Sensing, 16, 17,3391-3408, 1995.*

Vihma, T., J. Launiainen, and J. Uotila, Weddell Sea ice Drift: Kinematics and Wind Forcing, *J. Geophys. Res.*, 101, C8, 18279-18296, 1996.

White, W .B., and R.G. Petersen, An Antarctic Circumpolar Wave in Surface Pressure, Wind, Temperature and Sea-Ice Extent, *Nature,* 380,699-702, 1996.

10. Figures

Figure 1. Operational Antarctic ERS, J-ERS and RADARSAT receiving stations

Figure 2. Map indicating the location of ERS- 1 SAR image frames used in the Weddell Sea backscatter analysis. BackScatter distribution data from the bold SAR frames are described in the text (see Table 1).

Figure 3. (a) Photograph pancake ice field on 13 June, 1992; (b) sea-ice sample at this location at site N04E501 [after Drinkwater and Haas, 1994]; and (c) shipborne scatterometer scan at this site location, together with contrasting scan from 14 June and EScat σ^o_{Scatt} measurement. in the same location, '

Figure 4, SAR backscatter pdf's for each individual scenes, and for the entire grouped winter SAR dataset (see Figure 2. and Table 1 for SAR scenes) in black.

Figure 5. Mean WWGS '92 shipborne scatterometer ice signatures, from (a) white ice, (b) smooth first-year ice; (c) rough first-year ice; and (d) multiyear ice. Curves are fitted exponentially and error bars indicate the standard error of the data. Vertical lines delineate the incidence angle range of ERS SAR (20° $\leq \theta \leq$ 26°) and overlapping shaded pdf's show the probability distribution from SAR pixel samples in the locations of shipborne scatterometer measurements. A range of observed SAR values is shown for all sampled images for each ice type.

Figure 6. ERS-1 SAR image from orbit 52.49, frame 4941, taken on 17 July, 1992 [© ESA, 1992] and located in Figure 2. Boxes highlight regions from which component backscatter distributions are plotted in section 4.1.2. The inset marks the location of the image with respect to the track location of the research icebreaker *Polarstern.*

Figure 7. Summary plot of C-band Weddell Sea ice and ocean signatures, indicating the ranges and/or standard deviation of SAR, and shipborne (σ^o_{Ship}) and EScat (σ^o_{EScat}) backscatter coefficient measurements of each broad ice category.

Figure 8. Classified weekly mean SIRF *A* images in the ERS-1 Scatterometer mode, for (a) June 16 (i.e. days 165-171), 1992; and (b) 31 July (i.e. days 210 - 216), 1992. [ERS-1 Scatterometer data@ ESA].

Figure 9. Auto-covariance functions and normalized variance spectra of Argos-derived ice drift and wind speeds for free drifting buoy in the central Weddell Sea during WWGS'92.

Figure 10. Auto-covariance functions and normalized variance spectra of GPS-derived ice drift and wind speeds for Ice Station Weddell.

Figure 11. Examples of AVHRR Channel 4 derived sea-ice velocity fields for the 1992 periods; (a) 07:27-21:31 hrs on 10 June; (b) 21:31 hrs on 10 June to 21:07 hrs on 11 June; (c) 21:07 hrs on 11 June to 07:51 on 21 June.

Figure 12. 3-day ice motion vectors superimposed onto an ERS-1 SAR image for 15 March 1992 [Image © ESA, 1992]. The scale indicates the distance (in km) of the vector displacements and the mean u and v components of ice velocity are given at upper left [after DrinkWater, *In Prep].*

Figure 13. SAR-derived ice motion superimposed on the WWGS '92 buoy drift array, for periods (a) 14-17 July, 1992, and (b) 13-16 July. Gridded geostrophic winds and mean

climatological geostrophic currents are shown together with the optimally interpolated ECMWF pressure field. Buoy start locations are identified by ' ♦' symbols.

Figure 14. Color-coded display of deformation angle θ (*i.e.* tan"' E_T/E_1) superimposed upon the SAR image shown in Figure 12.

Figure 15. Comparison of SAR-tracked 3-day velocities with equivalent 3-day velocities computed from instantaneous GPS locations of Ice Station Weddell. A curl y arrow signifies points extracted from velocity fields exhibiting a high degree of vorticity.

Figure 16. Timeseries of ERS- 1 SAR-tracked IS W ice motion results. (a) shows measured surface windspeed (dotted) and 3-d smoothed windspeed; (b) shows SAR (dotted) and GPS-derived (solid) u component of velocity (i.e. west is positive); (c) v components of velocity (north positive) from SAR (dotted) and GPS (solid - 3-d running mean).

Figure 17. Seasonal SAR backscatter probability distribution functions. Bimodal peaks in winter distribution comprise first-year or seasonal (FY), and multiyear (MY) or perennial ice.

Figure 18. Timeseries of (a) surface air temperatures from the Finnish Salargos buoy; (b) snow-temperature gradients at thermistor sites on snow-covered perennial ice floes; (c) ■ or $\bar{\sigma}^o_{MY}$ of multiyear floes (vertical bars indicating range of values), x or (i.e. global SAR image means), and . $\bar{\sigma}^o_{Scatt}$ or 40° incidence normalized backscatter coefficient; (d) ♦ - EScat backscatter gradient *M* (linear regressed) at 40° incidence [after Drinkwater and Lytle, *In* Press].

11. Tables

Table 1. List of ERS-1 SAR image frames used in regional backscatter data analysis (see Figure 2 for geographic locations in the Weddell Sea).

Image (orbit/frame)	Date and Time (UTC)	Center Latitude	Center Longitude
50905121	**6 July 92:09:01:35.786**	**-72.263**	**343.424**
52494941	**17 July 92:11:34:19.254**	**-64.706**	**318.550**
53775031	**26 July** 92:10:12:16.392	-68.614	333.541
53875949	27 July 92:03:11:05.712	-60.406	310.928
53875967	27 July 92:03:11:20.807	-59.581	310.165
54495139	31 July 92:10:56:54.090	-72.934	312.629

Table 2. Summary of backscatter samples from ERS-1 SAR image 5249/4941 in Figure 6.

Ice Type	Sample #	Mean/Median (dB)	Std. Deviation (dB)
Smooth First-Year	FYS 1	-16.09/-16.10	*0.99
	FYS 2	-15.46/-15.50	*1.05
Rough First-Year	FYR 1	-10.14/-10.30	±1.83
	FYR 2	-9.54/-9.5	±1.69
Multiyear Ice	MY 1	-5.72/-5.50	*1.88
	MY2	-6.81/-6.50	±2.27
	MY 3	-5.92/-5.50	±2.03

Table 3. Summary of winter C-band EScat backscatter ranges ($\theta = 40°$ incidence) of main categories of sea ice in the Weddell Sea.

Ice Type	Backscatter Range
Icebergs	$-6.0 \leq \sigma^0 \leq 0.0$
Multiyear/Pancakes	$-11.0 \leq \sigma^0 < -6.0$
Rough First-year	$-14.0 \leq \sigma^0 < -11.0$
Smooth First-year	$-20.0 \leq \sigma^0 < -14.0$
Nilas	$-32.0 \leq \sigma^0 < -20.0$

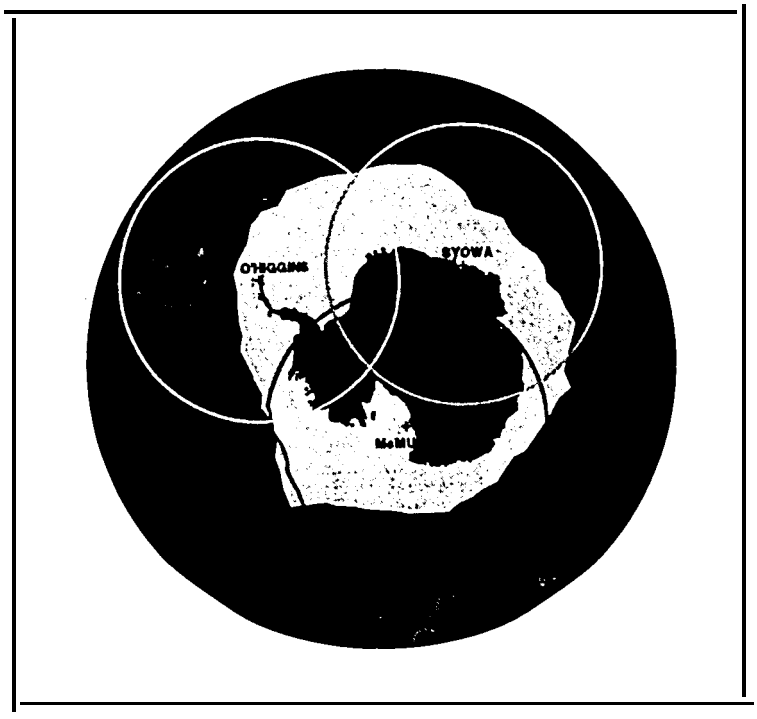

Figure 1. Operational Antarctic ERS, J-ERS and RADARSAT receiving stations together with their respective regions of direct data acquisition.

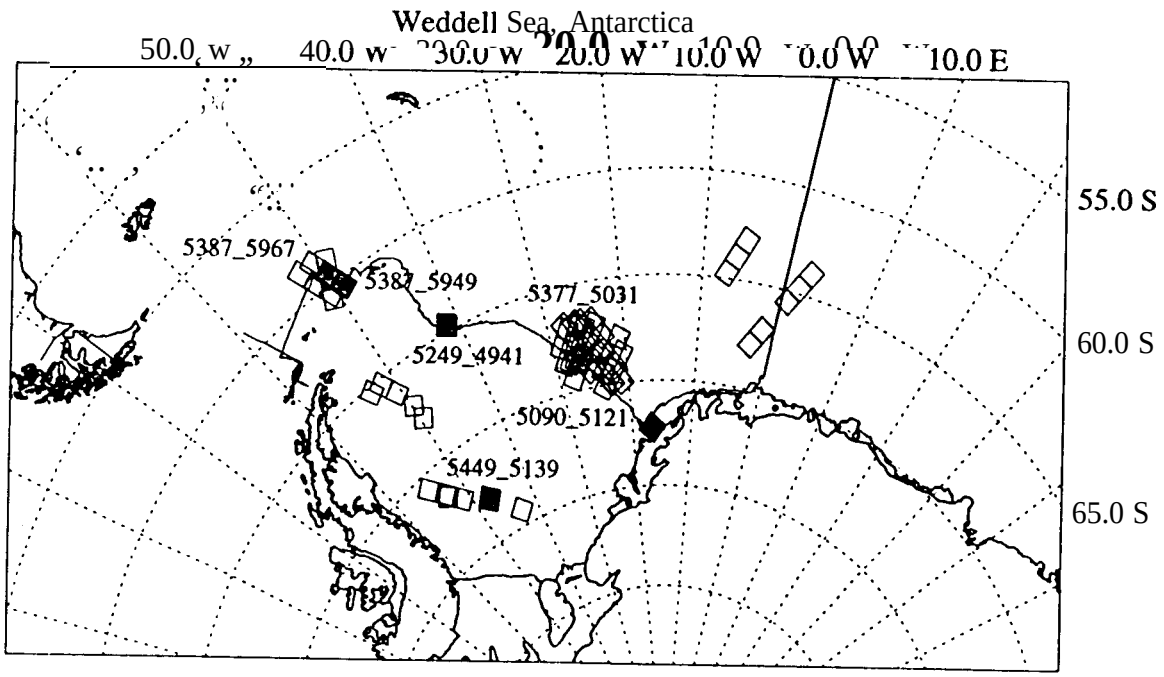

Figure 2. **Map indicating the location of ERS- 1 SAR image frames used** in the Weddell Sea backscatter analysis. Backscatter distribution data from the bold SAR frames are shown in Figure 4 (see Table 1 for frame listing).

a.

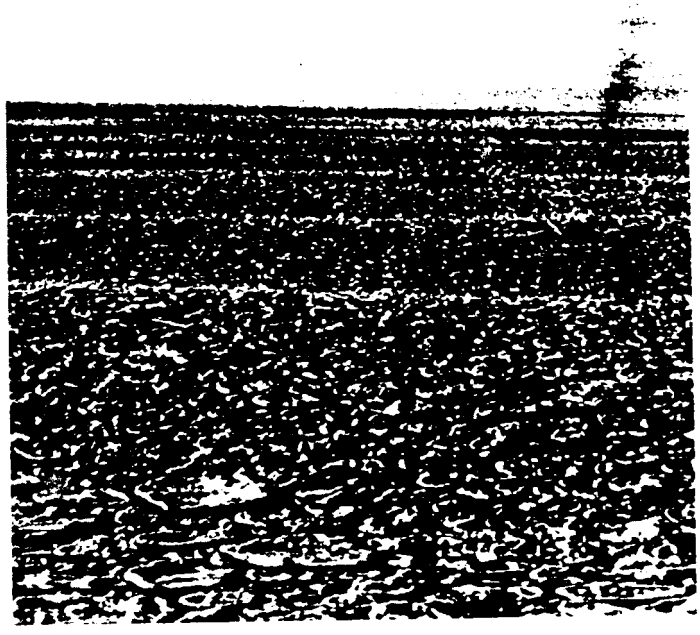

b.

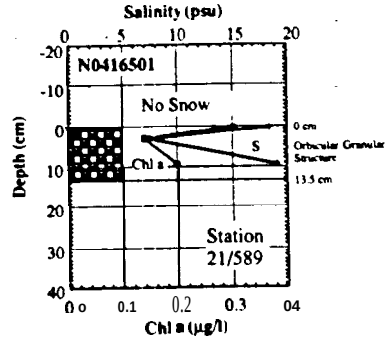
Salinity (psu)
0
5
10
15
20
-20
-10
0
10
20
30
40
N0416501
No Snow
S
Chl a
0 cm
Orbicular Granular Structure
13.5 cm
Station
21/589
Depth (cm)
0.0
0.1
0.2
0.3
0.4
Chl a (µg/l)

c.

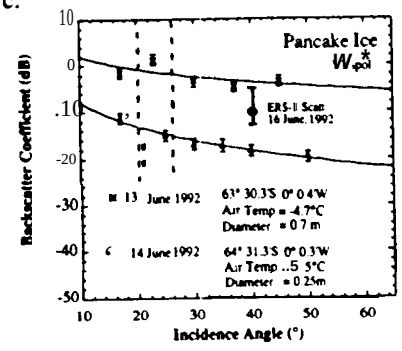
10
0
-10
-20
-30
-40
-50
Pancake Ice
W_{vpol}^{*}
ERS-1 Scat
16 June 1992
13 June 1992
63° 30.3'S 0° 0.4'W
Air Temp = -4.7°C
Diameter = 0.7 m
14 June 1992
64° 31.3'S 0° 0.3'W
Air Temp ..5 5°C
Diameter = 0.25m
Backscatter Coefficient (dB)
10
20
30
40
50
60
Incidence Angle (°)

FIGURE 3.

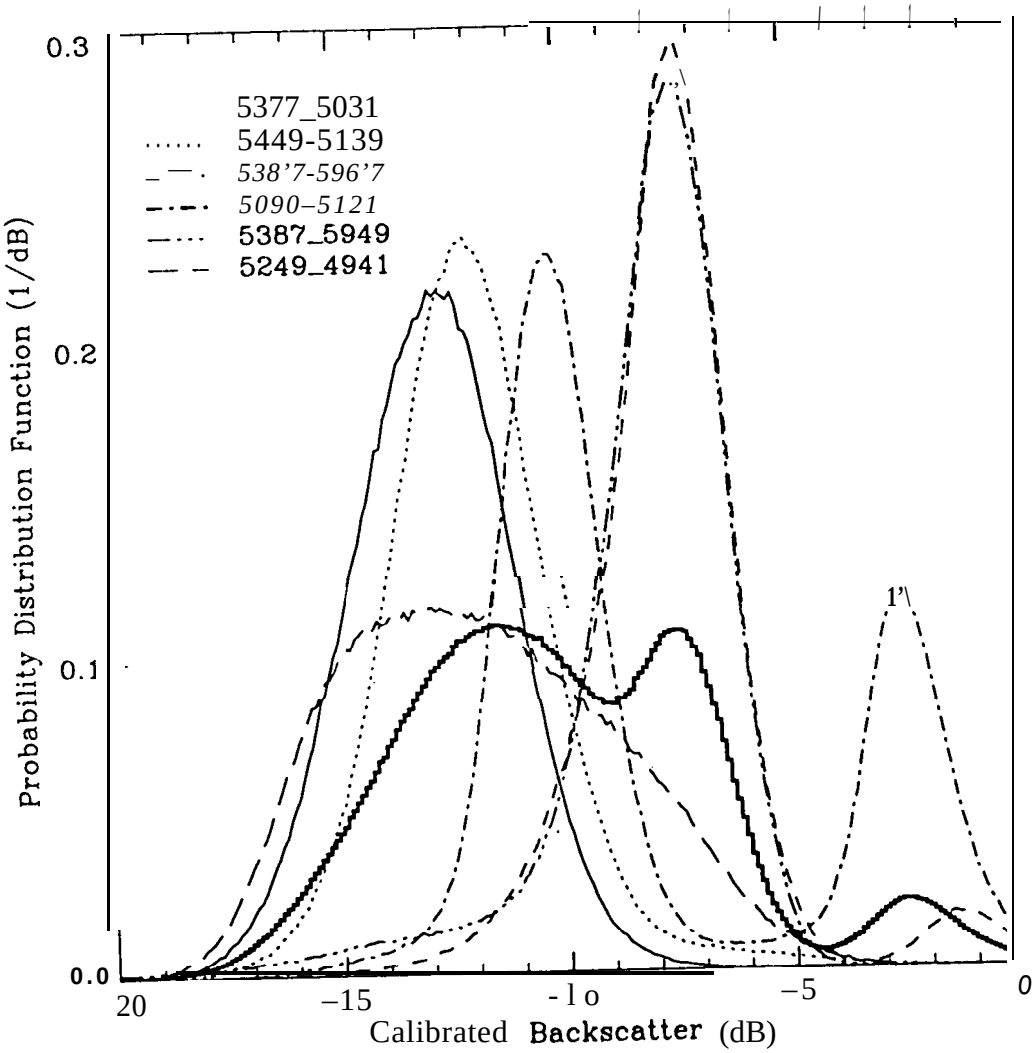
0.3
0.2
0.1
0.0
Probability Distribution Function (1/dB)
5377_5031
5449-5139
538'7-596'7
5090–5121
5387_5949
5249_4941
1'
20
–15
-1o
–5
0
Calibrated Backscatter (dB)

FIGURE 4.

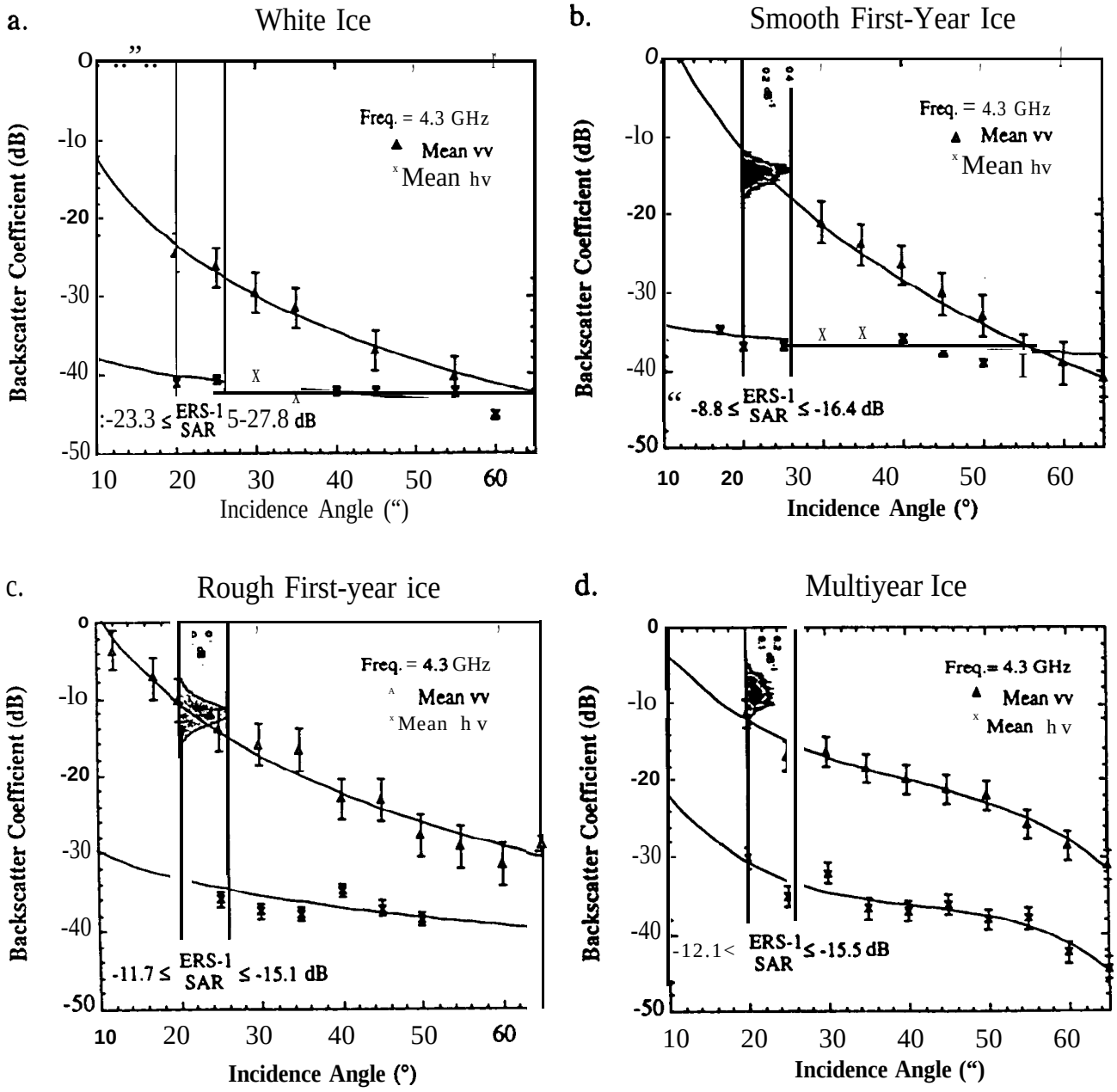
a.
White Ice
Freq. = 4.3 GHz
Mean vv
Mean hv
:-23.3 ≤ ERS-1 SAR 5-27.8 dB
Backscatter Coefficient (dB)
Incidence Angle (“)
b.
Smooth First-Year Ice
Freq. = 4.3 GHz
Mean vv
Mean hv
-8.8 ≤ ERS-1 SAR ≤ -16.4 dB
Backscatter Coefficient (dB)
Incidence Angle (°)
c.
Rough First-year ice
Freq. = 4.3 GHz
Mean vv
Mean hv
-11.7 ≤ ERS-1 SAR ≤ -15.1 dB
Backscatter Coefficient (dB)
Incidence Angle (°)
d.
Multiyear Ice
Freq.= 4.3 GHz
Mean vv
Mean hv
-12.1< ERS-1 SAR ≤ -15.5 dB
Backscatter Coefficient (dB)
Incidence Angle (“)

FIGURE 5.

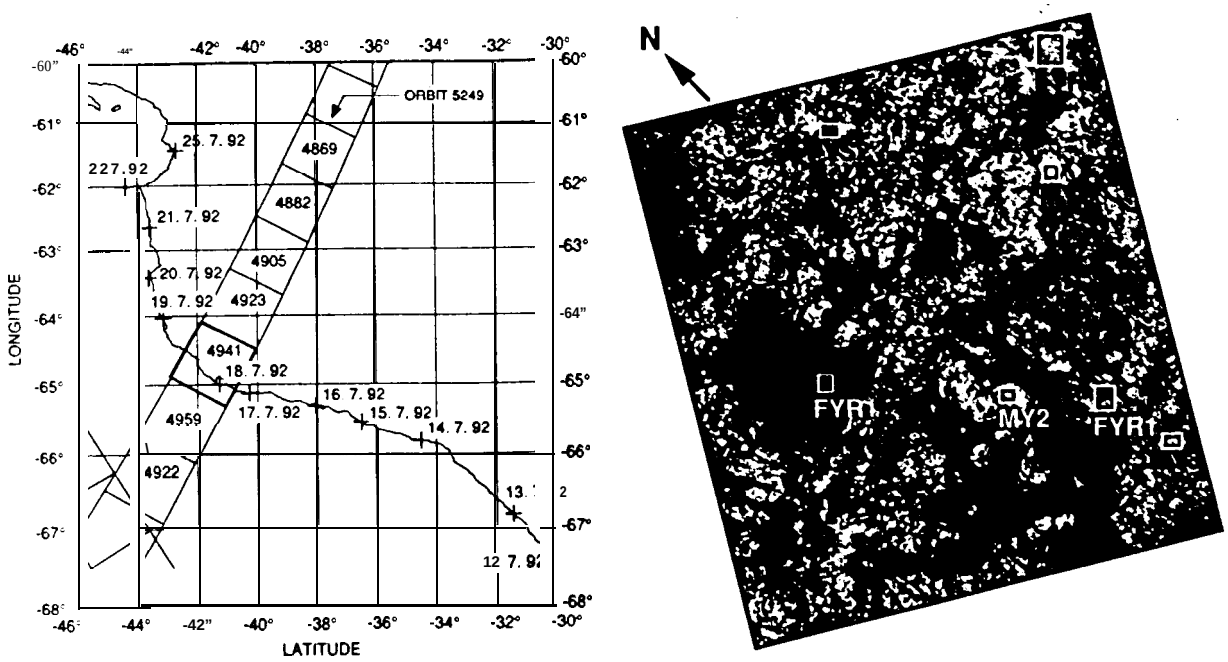
ORBIT 5249
25. 7. 92
227.92
21. 7. 92
20. 7. 92
19. 7. 92
18. 7. 92
17. 7. 92
16. 7. 92
15. 7. 92
14. 7. 92
4869
4882
4905
4923
4941
4959
4922
LONGITUDE
LATITUDE
N
FYR1
MY2
FYR1

FIGURE 6

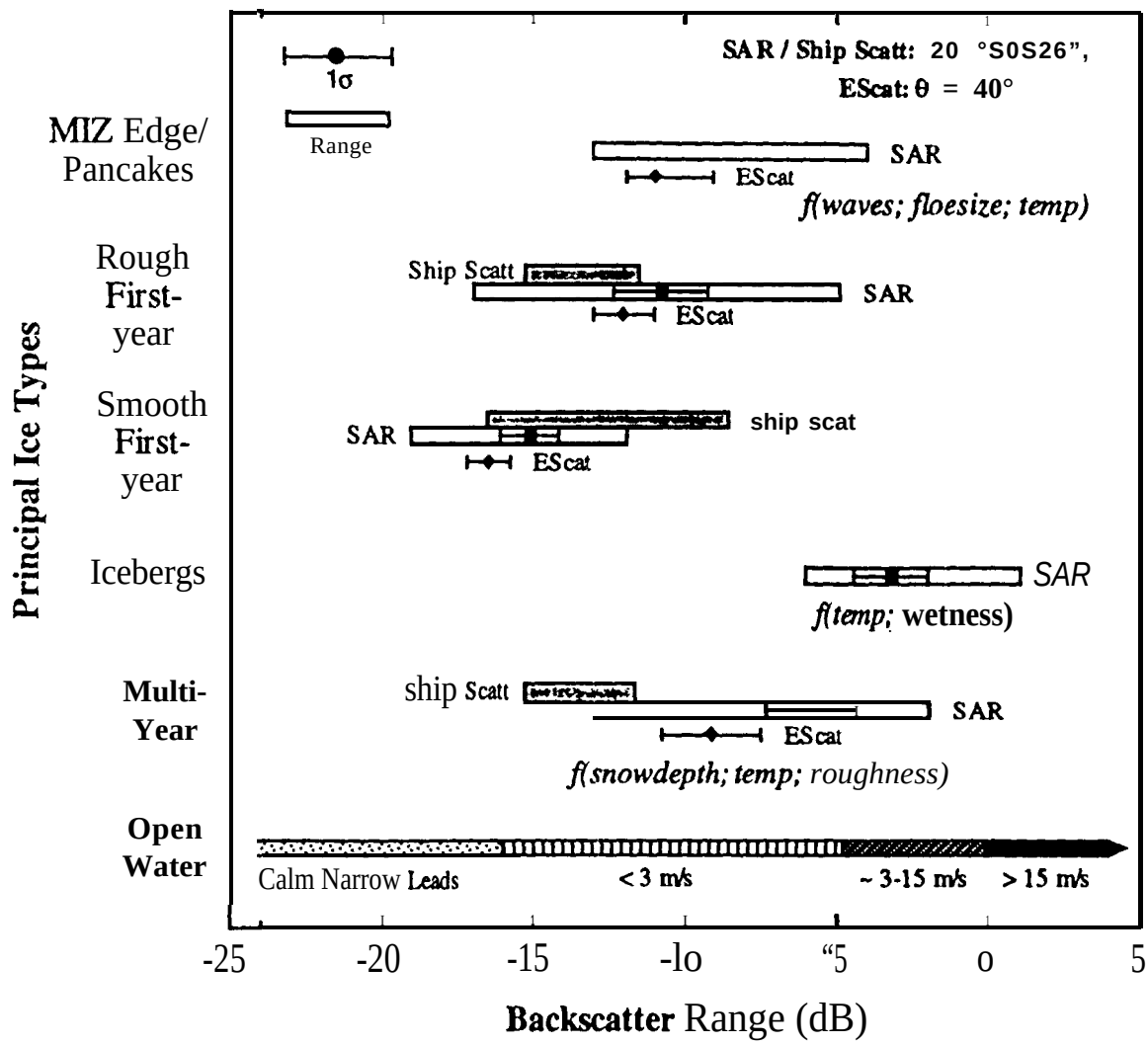
SAR / Ship Scatt: 20 °S0S26",
EScat: θ = 40°
1σ
Range
MIZ Edge/ Pancakes
SAR
EScat
f(waves; floesize; temp)
Rough First-year
Ship Scatt
SAR
EScat
Smooth First-year
SAR
ship scat
EScat
Icebergs
SAR
f(temp; wetness)
Multi-Year
ship Scatt
SAR
EScat
f(snowdepth; temp; roughness)
Open Water
Calm Narrow Leads
< 3 m/s
~ 3-15 m/s
> 15 m/s
Principal Ice Types
-25
-20
-15
-lo
"5
o
5
Backscatter Range (dB)

FIGURE 7

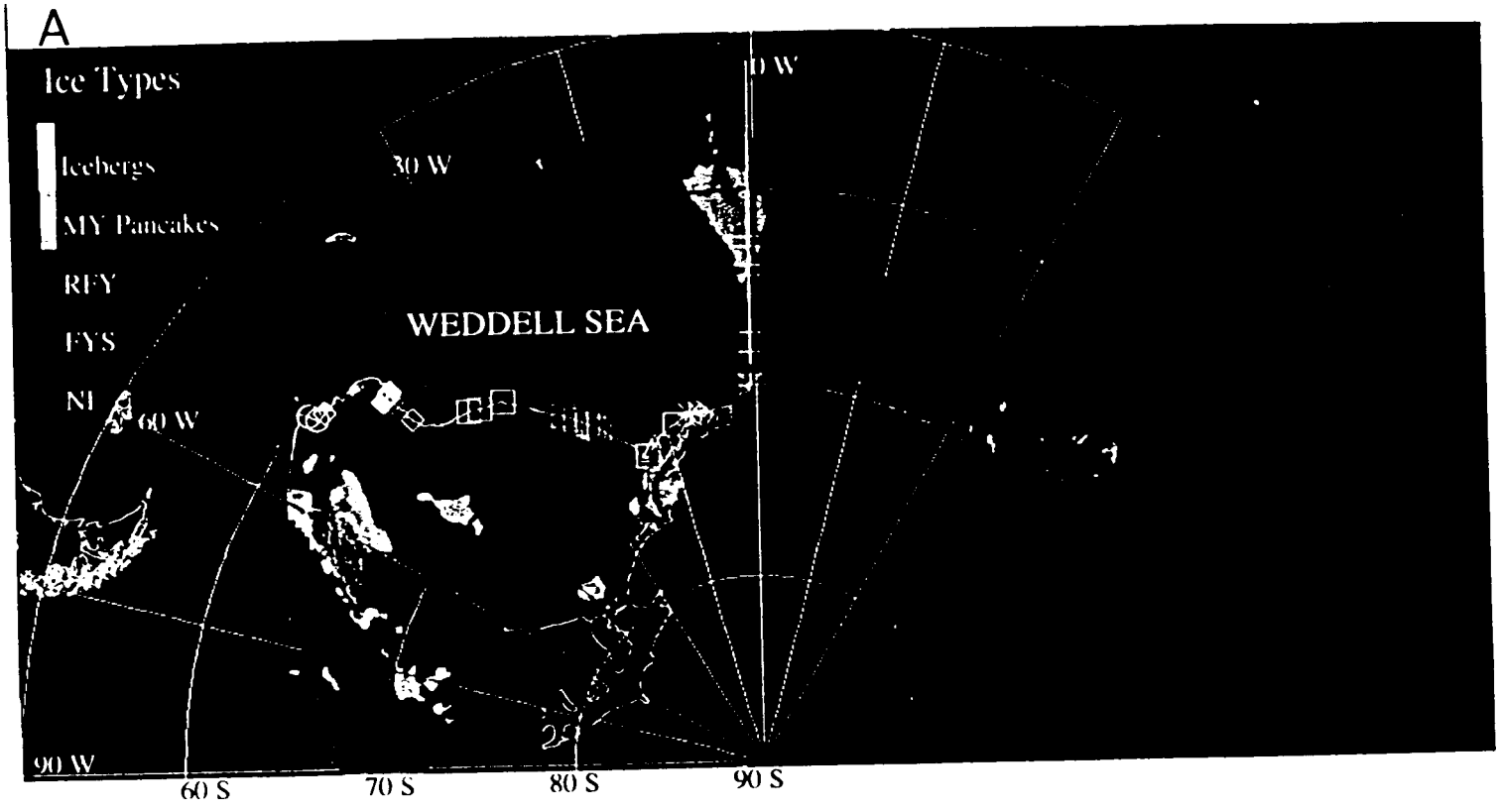
A
Ice Types
Icebergs
MY Pancakes
RFY
FYS
NI
WEDDELL SEA
0 W
30 W
60 W
90 W
60 S
70 S
80 S
90 S

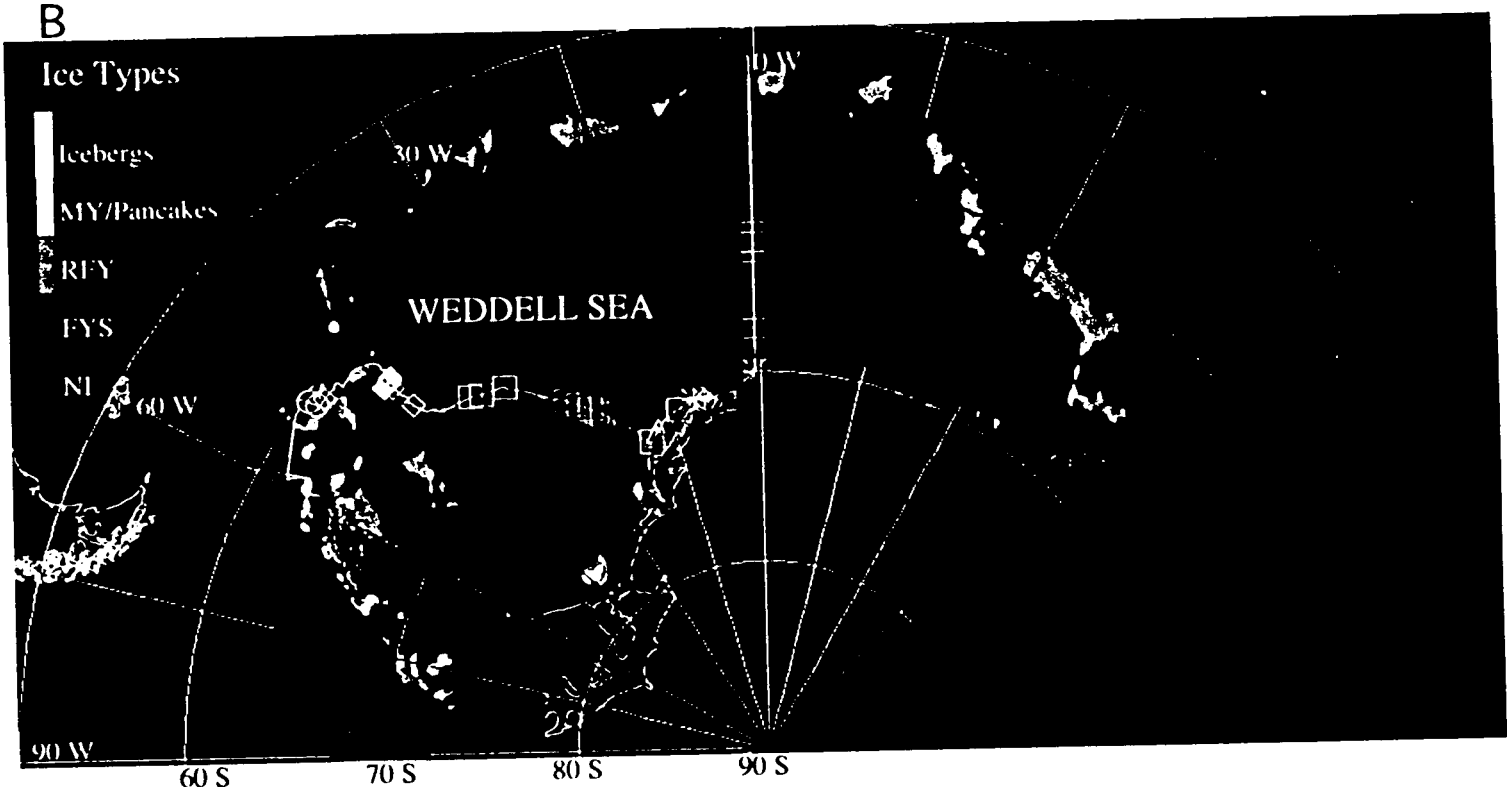
B
Ice Types
Icebergs
MY/Pancakes
RFY
FYS
NI
WEDDELL SEA
0 W
30 W
60 W
90 W
60 S
70 S
80 S
90 S

FIGURE 8

Ice motion correlational analysis.
Modal velocity.

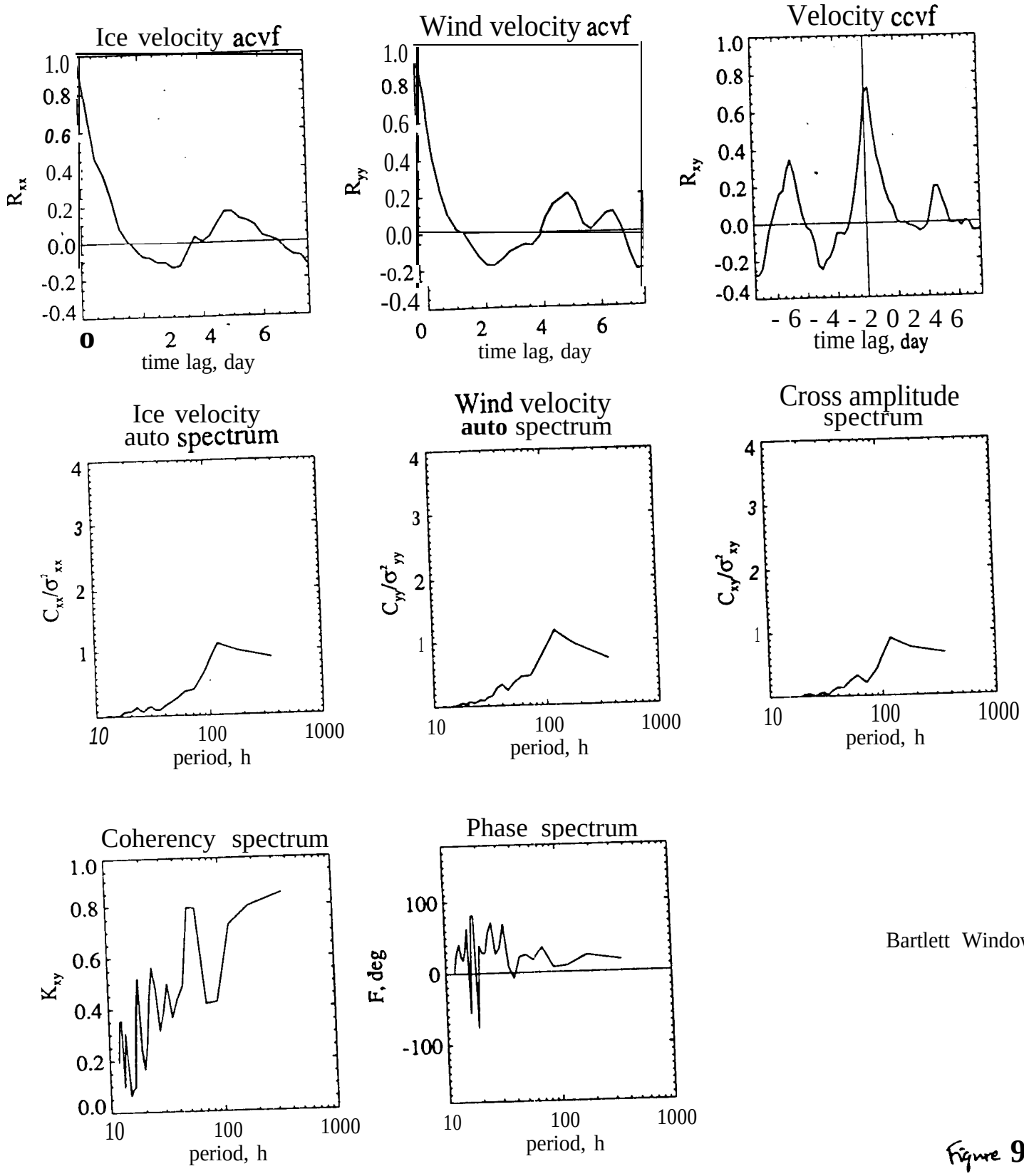

Bartlett Windowing

Figure 9

Ice motion correlational analysis.
Modal velocity.

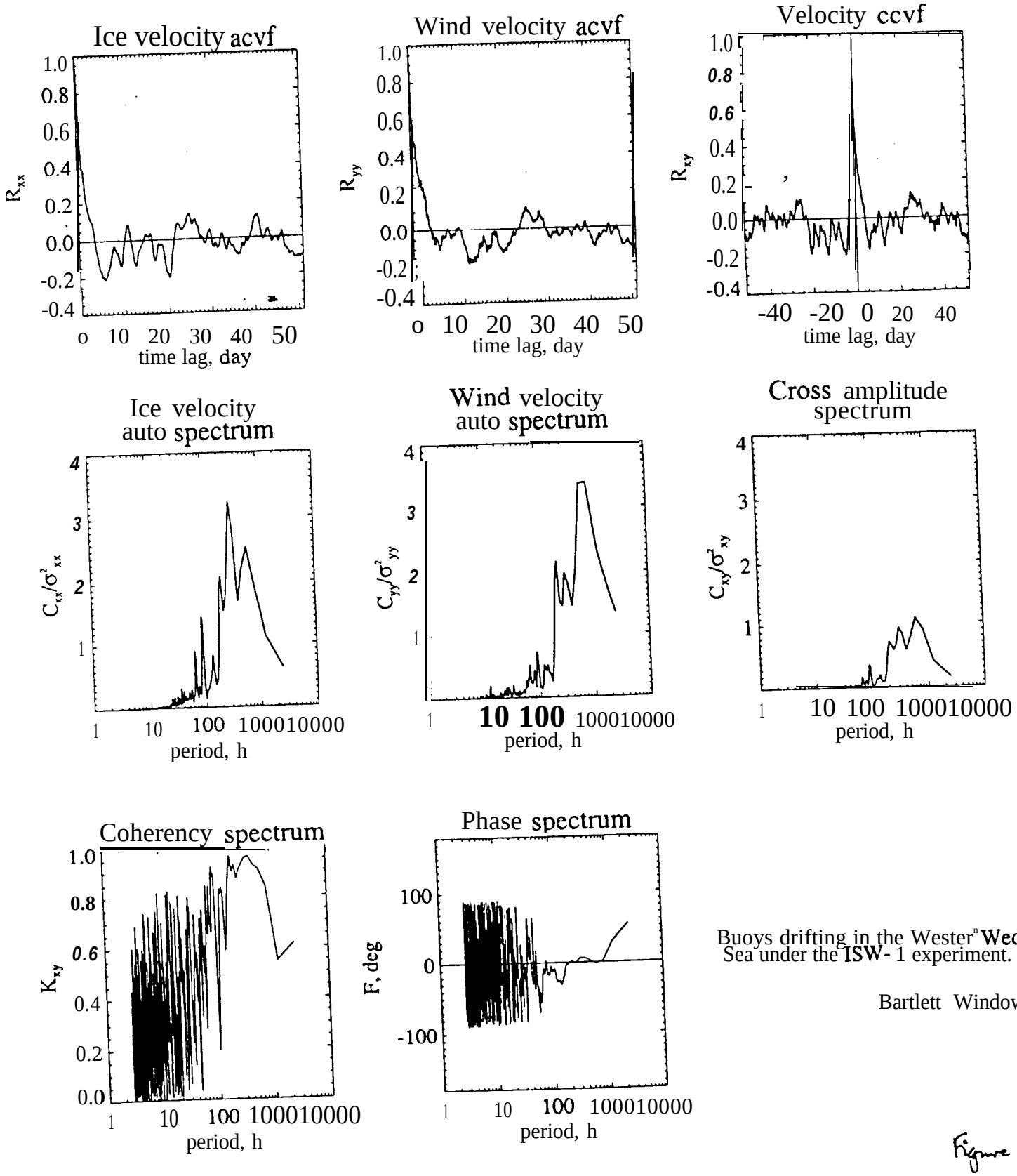

Buoys drifting in the Western Weddell Sea under the ISW-1 experiment.

Bartlett Windowing

Figure 10.

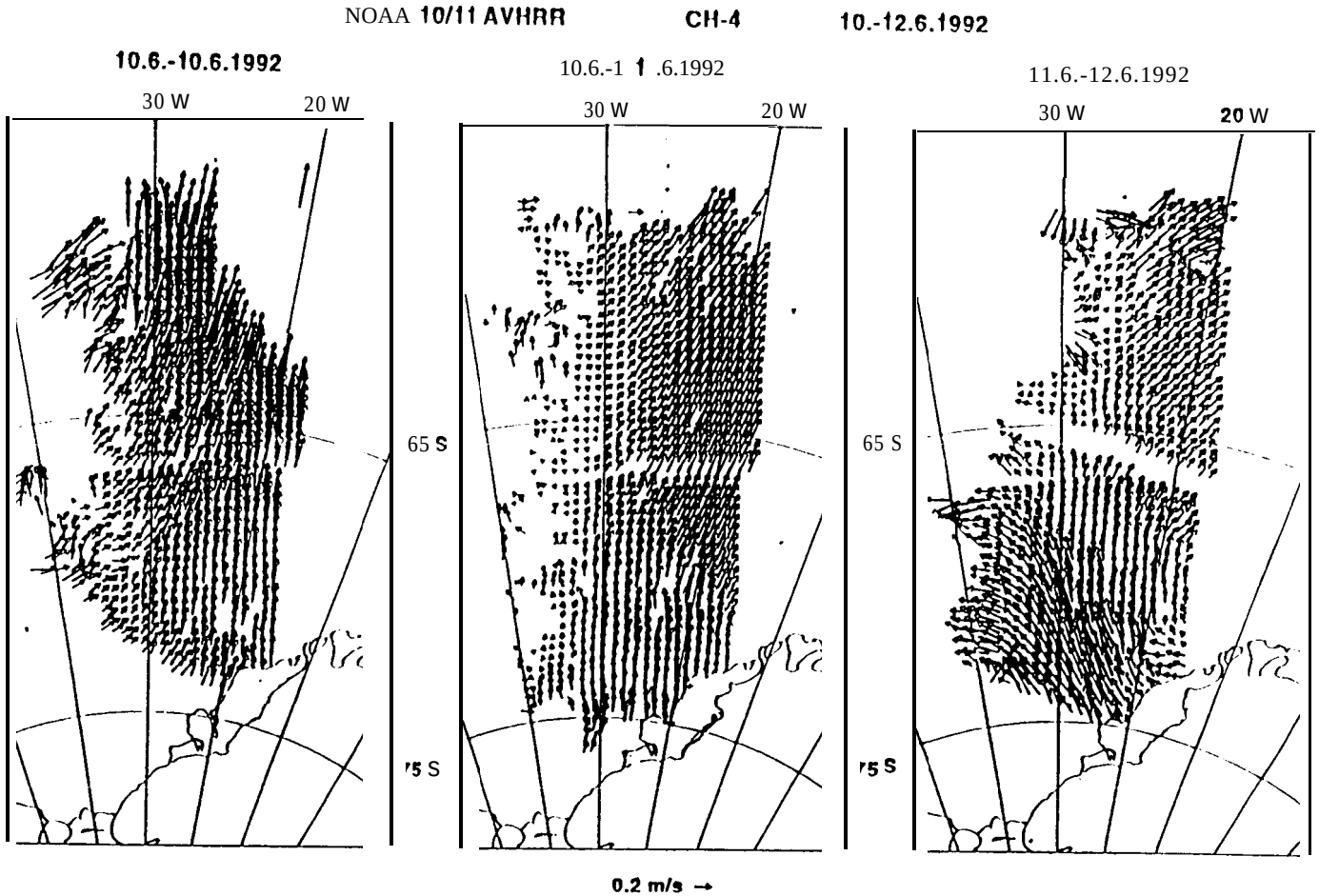

Figure 11 Examples of AVHRR derived seaice velocity fields for the period 10.6.-12.6,1992.

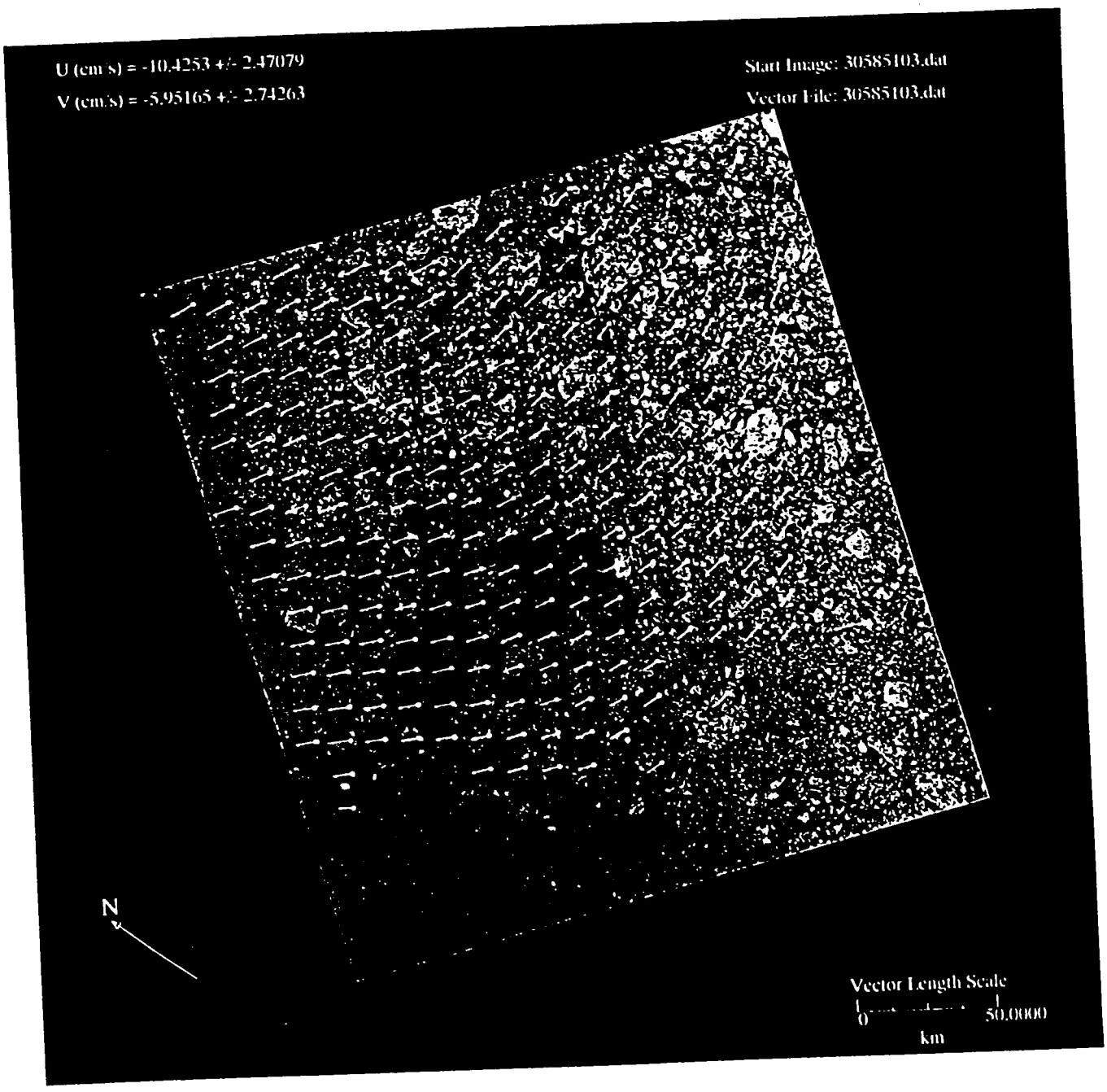
U (cm/s) = -10.4253 +/- 2.47079
V (cm/s) = -5.95165 +/- 2.74263
Start Image: 30585103.dat
Vector File: 30585103.dat
N
Vector Length Scale
0
50.0000
km

FIGURE 12

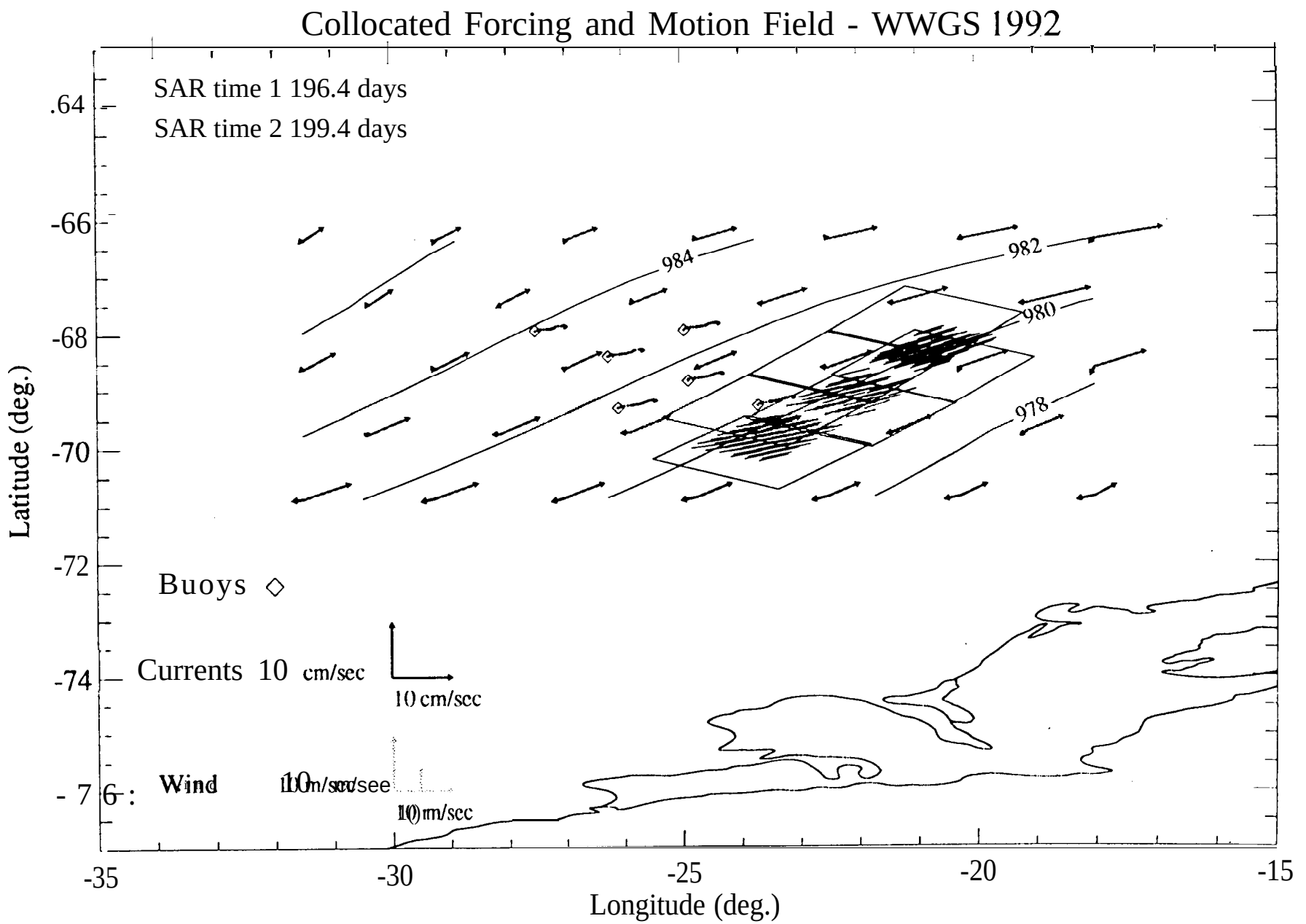
Collocated Forcing and Motion Field - WWGS 1992
SAR time 1 196.4 days
SAR time 2 199.4 days
984
982
980
978
Buoys ◇
Currents 10 cm/sec
10 cm/sec
Wind
10 m/sec
Latitude (deg.)
Longitude (deg.)
.64
-66
-68
-70
-72
-74
-35
-30
-25
-20
-15

FIGURE 13a

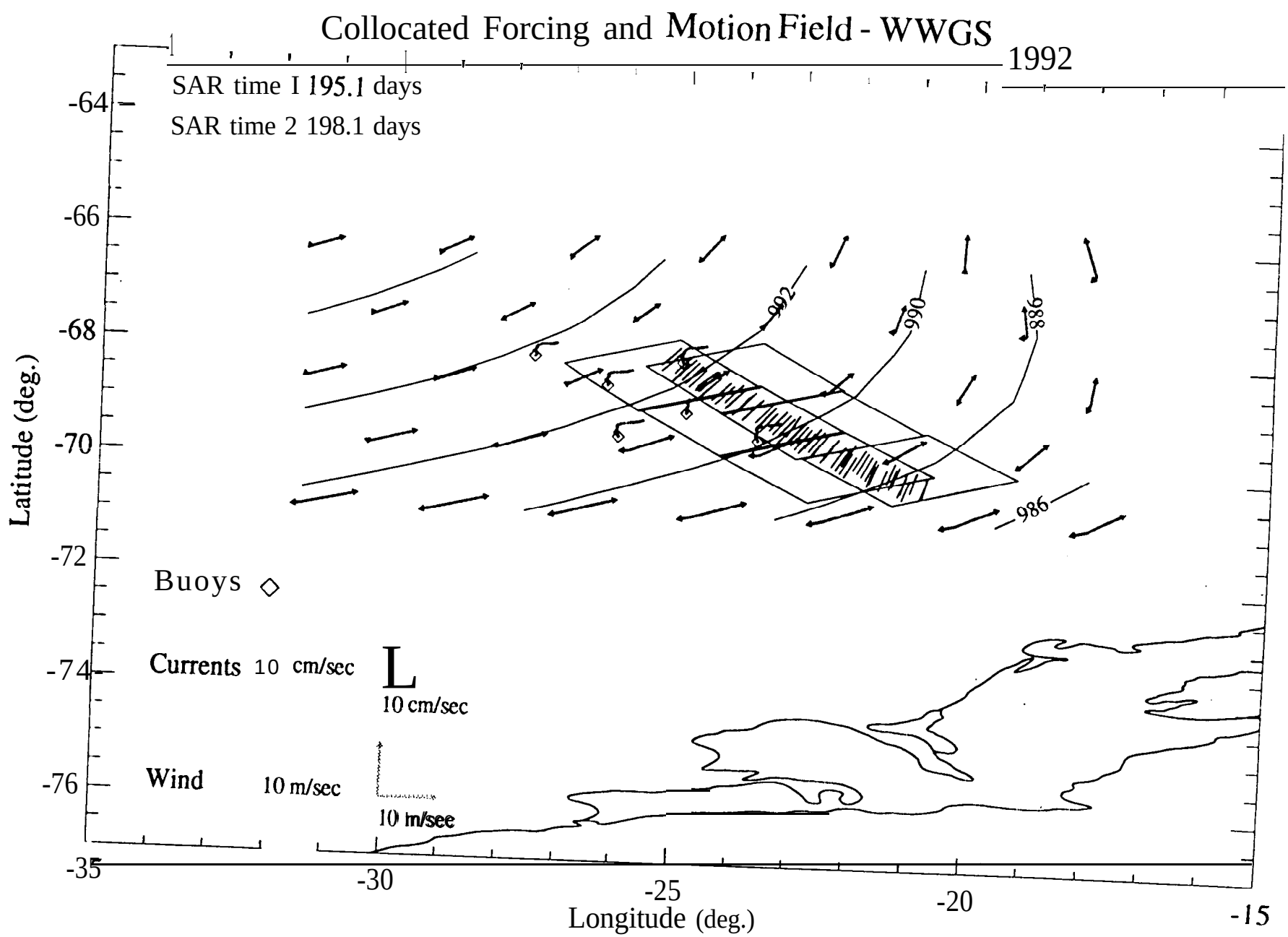
Collocated Forcing and Motion Field - WWGS
1992
SAR time I 195.1 days
SAR time 2 198.1 days
992
990
988
986
Buoys
Currents 10 cm/sec
10 cm/sec
Wind 10 m/sec
10 m/see
-64
-66
-68
-70
-72
-74
-76
Latitude (deg.)
-35
-30
-25
-20
-15
Longitude (deg.)

FIGURE 12b

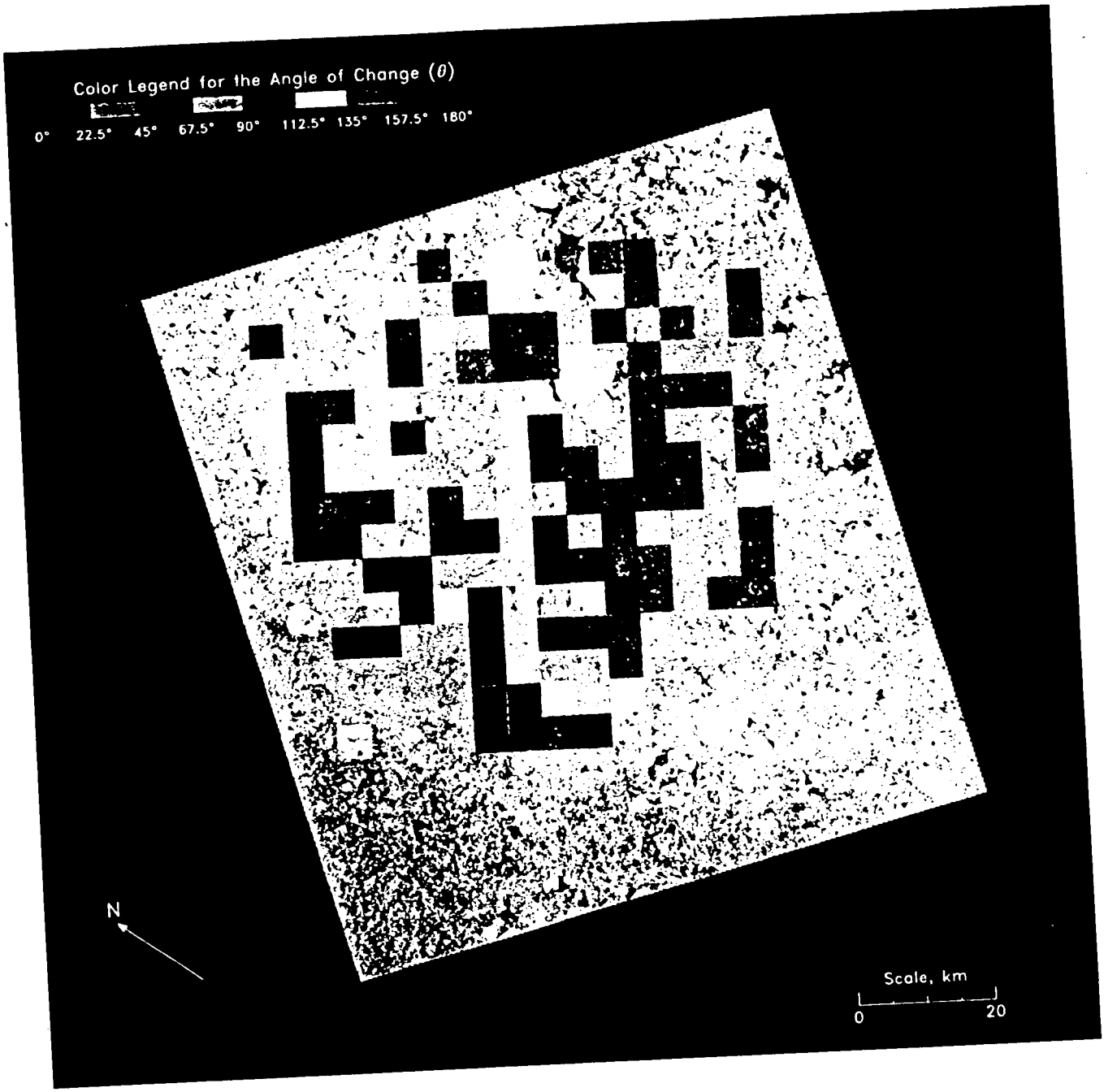
Color Legend for the Angle of Change (θ)
0° 22.5° 45° 67.5° 90° 112.5° 135° 157.5° 180°
N
Scale, km
0
20

FIGURE 14.

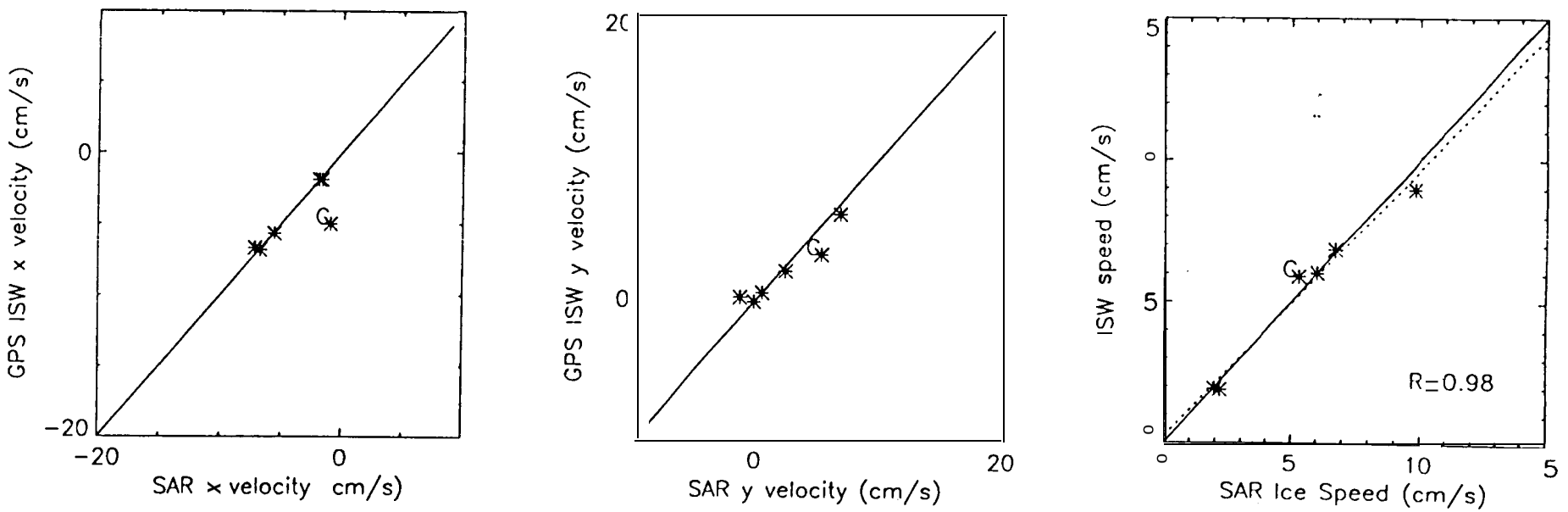
GPS ISW x velocity (cm/s)
0
−20
−20
0
SAR x velocity cm/s)
G
GPS ISW y velocity (cm/s)
20
0
0
20
SAR y velocity (cm/s)
G
ISW speed (cm/s)
5
0
5
0
0
5
10
5
SAR Ice Speed (cm/s)
G
R=0.98

FIGURE 15

a.

b.

c.

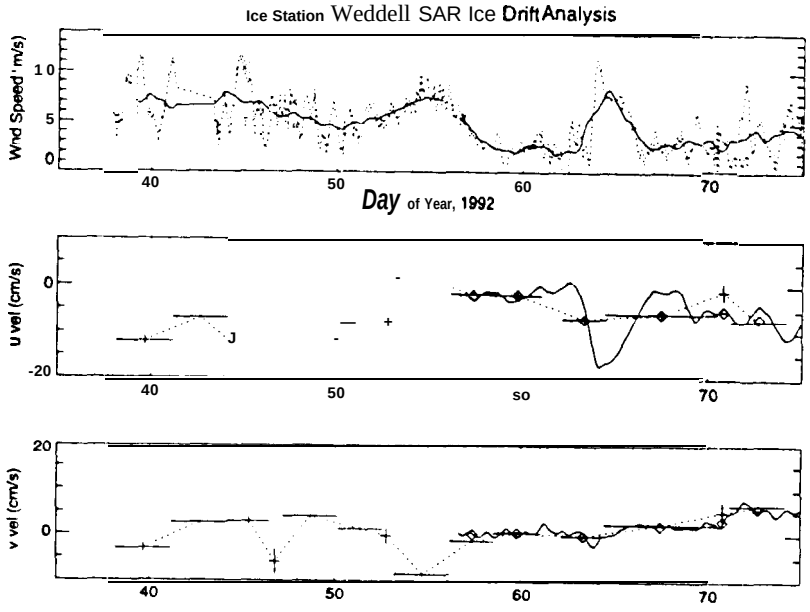

FIGURE 16.

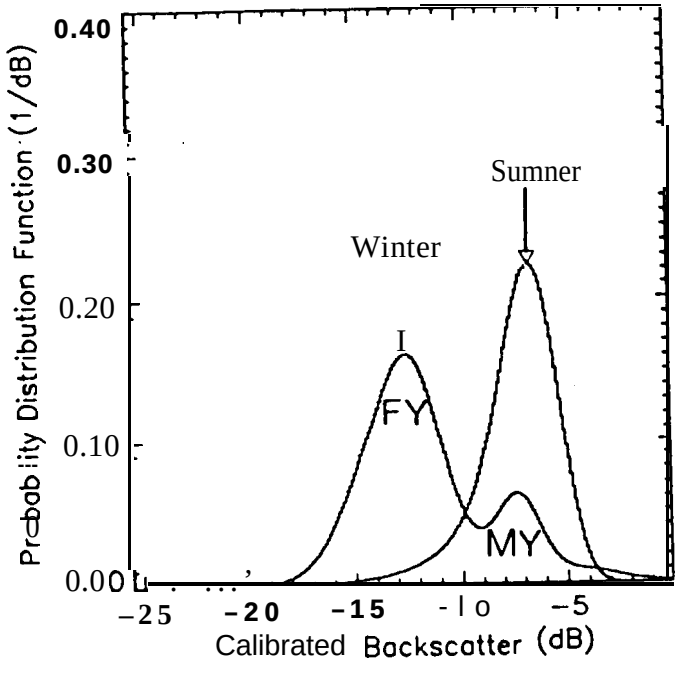
0.40
0.30
0.20
0.10
0.00
Probability Distribution Function (1/dB)
Sumner
Winter
FY
MY
-25
-20
-15
-10
-5
Calibrated Backscatter (dB)

FIGURE 17

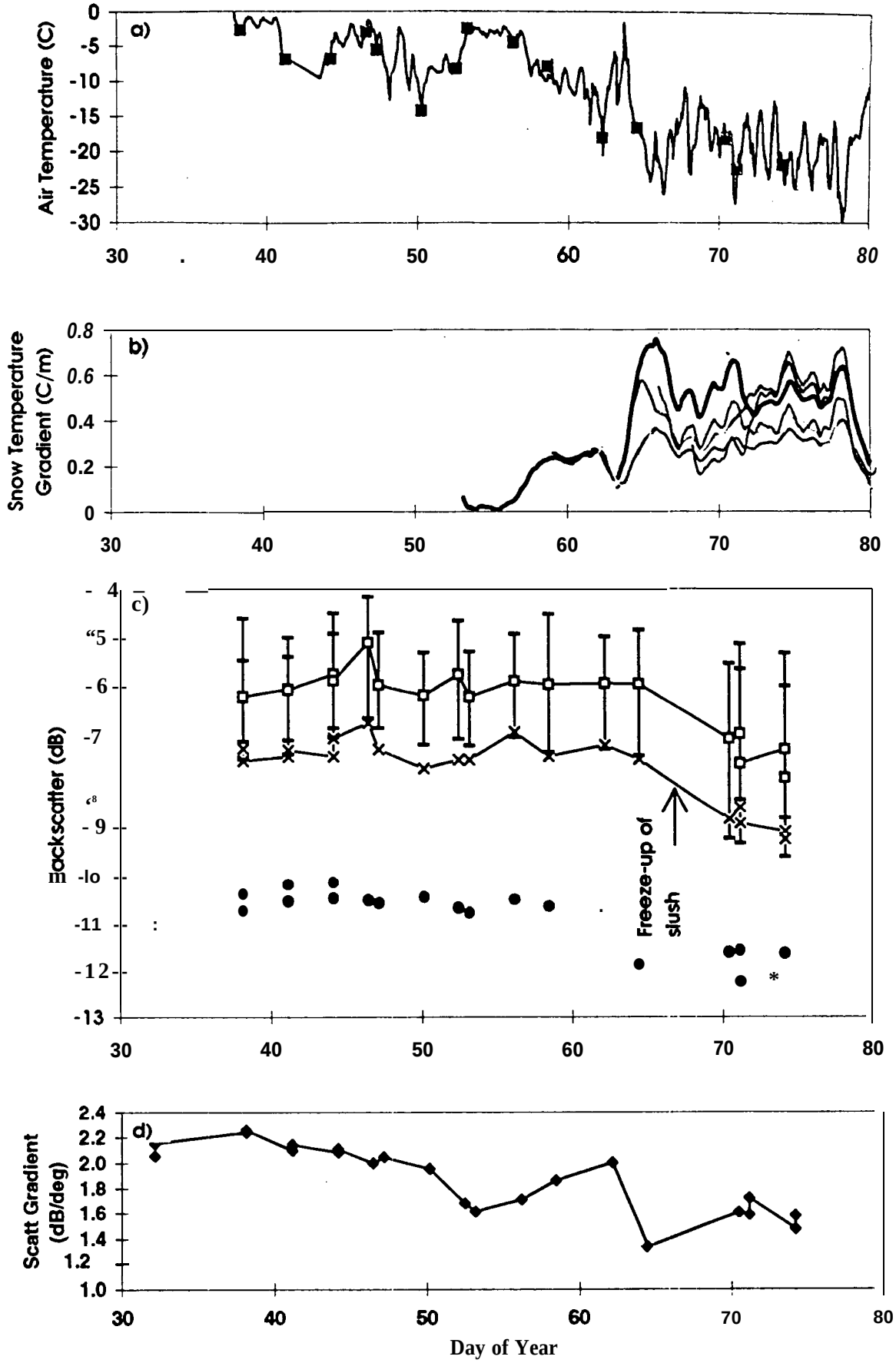
a)
Air Temperature (C)
0
-5
-10
-15
-20
-25
-30
30
40
50
60
70
80
b)
Snow Temperature Gradient (C/m)
0.8
0.6
0.4
0.2
0
c)
Backscatter (dB)
-4
-5
-6
-7
-9
-10
-11
-12
-13
Freeze-up of slush
d)
Scatt Gradient (dB/deg)
2.4
2.2
2.0
1.8
1.6
1.4
1.2
1.0
Day of Year

FIGURE 18.